Enhancement of performance of Wave Turbine during Stall Using Passive Flow Control: First and Second Law Analysis

Ahmed S. Shehata[1, 2*], Qing Xiao [1], Mohamed M. Selim[2], A. H. Elbatran[2], Day Alexander [1]

1) Department of Naval Architecture, Ocean and Marine Engineering, University of Strathclyde, Glasgow G4 0LZ, U.K

2) College of Engineering and Technology, Arab Academy for Science Technology and Maritime Transport, P.O. 1029 AbuQir, Alexandria, EGYPT

**** Corresponding Author**: Ahmed S. Shehata,*

***E-mail address**: ahmed.mohamed-ahmed-shehata@strath.ac.uk*

ABSTRACT

Wells turbine is the most common type of self-rectifying air turbine employed by Oscillating Water Column (OWC) wave energy devices due to its technical simplicity, reliability, and design robustness. Because it subjected to early stall, there were many endeavors to improve the energy extraction performance of Wells turbine within the stall regime. Using the multi suction slots as a passive flow control can help obtaining a delayed stall. Two, three and four suction slots were investigated to improve the performance of Wells turbine in the stall regime. In addition the commonly used first law analysis, the present study utilized an entropy generation minimization method to examine the impact of the multi suction slots method on the entropy generation characteristics around the turbine blade. The turbine blade with optimum suction slots number and location was investigated using the oscillating water system based on the real data from the site. To achieve this purpose, two-dimension numerical models for Wells turbine airfoils under sinusoidal wave flow conditions were built and analyze using (ANSYS FLUENT) solver. It is found that the airfoil with three suction slots located at 40%, 55% and 90% from leading edge in chord percentage give the highest torque coefficient by 26.7% before the stall and 51% after the stall.

Keywords: Oscillating flow; Wells turbine; Flow control method; Entropy generation; Egyptian Coasts.

1 Nomenclature

A	Total blade area (m^2)
c	Blade chord (m)
C_D	Drag force coefficient
C_L	Lift force coefficient
C_T	Torque coefficient
D	The fluid domain
D_{ss}	Suction slot diameter (m)
f	cycle frequency (Hz)
F_D	In-line force acting on cylinder per unit length (gf)
G	The filter function
KE	Kinetic Energy (W/K)
L_{ss}	Suction slot location from leading edge in chord percentage %
L_{Rss}	Reference suction slot location from leading edge in chord percentage %
K	Turbulent kinetic energy
Δp	Pressure difference across the turbine (N/m^2)
P_{ss}	Suction slot pitch distance on x axis
ΔP_{ss}	Minimum distance between any two suction slot on x axis
R_m	Mean rotor radius (m)
S_{gen}	local entropy generation rate (W/m^2K)
S_G	Global entropy generation rate (W/K)
S_{ij}	Mean strain rate
S_t	Thermal entropy generation rate (W/m^2K)
S_V	Viscous entropy generation rate (W/m^2K)
T_o	Reservoir temperature (K)

$\bar{u}_i$	Reynolds Averaged velocity component in i direction (m/s)
V	Volume of a computation cell
V_a	Instantaneous Velocity (m/s)
V_{am}	highest speed of axial direction (m/s)
V_o	Initial velocity for computation (m/s)
$\dot{W}$	The net-work transfer rate
W_{rev}	Reversible work
η_F	The efficiency in first law of thermodynamics
η_S	The second law efficiency
μ	Viscosity (Kg/ms)
μ_t	Turbulent viscosity
ρ	Density (Kg/m^3)
$\bar{\emptyset}$	Flow coefficient
ω	Rotor angular speed (rad/sec)
$\left(-\overline{\rho u_i' u_j'}\right)$	Reynolds stress tensor

1

List of Abbreviations	
CFD	Computational Fluid Dynamics
NACA	National Advisory Committee for Aeronautics
OWC	Oscillating Water Column
2D	Two Dimensional
3D	Three Dimensional

2 # 1. Introduction

3 Most of fixed-structure OWC systems are located on the shoreline or near the shore. Shoreline
4 devices are characterized by relatively easier maintenance and installation, and they do not require
5 deep water moorings and long underwater electrical cables. The floating OWC devices are slack-

moored to the sea bed and so are largely free to oscillate, enhancing the wave energy absorption if the device is properly designed for that purpose [1-6]. The energy conversion from the oscillating air column can be achieved by using a self-rectifying air turbine such as Wells turbine which was invented by A. A. Wells in 1976 [7-12]. The Wells turbine is one of the simplest and probably the most economical turbines for wave energy conversion. It does not require rectifying air valves and can extract power at a low airflow rate, when other turbines would be inefficient. Therefore, it has been extensively researched and developed in many countries. Most self-rectifying air turbines for wave energy conversion proposed and tested so far are axial-flow machines of two basic types: the Wells turbine and the impulse turbine. The impulse turbine was patented by I. A. Babintsev in 1975 [13]. Its rotor is basically identical to the rotor of a conventional single-stage steam turbine of axial-flow impulse type. Since the turbine is required to be self-rectifying, there are two rows of guide vanes, placed symmetrically on both sides of the rotor, instead of a single row. These two rows of guide vanes are the reflection of each other, with respect to a plane through the rotor disc [14-16]. Therefore, it is more complex and more costly than Wells turbine. The efficiency of Wells turbine is higher than that of the impulse turbine when the flow coefficient is less than the stall point. But after the stall point of Wells turbine, the efficiency of impulse turbine is considerably higher than that of Wells turbine. However, the peak efficiencies are almost the same [17].

There are several factors that influence the design, hence performance, of Wells turbine [3, 18, 19]. The optimization and improvement of such parameters aim mainly at overcoming the existing disadvantages of the system. The main disadvantage of Wells turbine is the stall condition [12, 17, 20]. At large flow rates with a large angle of attack, the boundary layers on the blades tend to separate, leading to a drop in torque coefficient and thus the efficiency. A further increase in the angle of attack, beyond the stall angle, will result in a decrease in lift and also a significant increase in drag. From references [1, 12, 17] it can be noted that Wells turbine can extract power at low air flow rate, when other turbines would be inefficient [15]. Also, the aerodynamic efficiency increases with the increase of the flow coefficient (angle of attack) up to a certain value, after which it decreases. Thus, most of the past studies aimed to improve the torque coefficient (the turbine output) and improve the turbine behavior under the stall condition.

The delay of stall onset contributes to improving Wells turbine performance can be achieved by setting guide vanes on the rotor's hub [18, 19]. The results of mathematical simulations considering several aerodynamic designs of the Wells turbine are shown in Table 1 [21]. Different guide vanes designs were compared and investigated analytically [22], taking into account the turbine starting characteristics and efficiency in irregular wave conditions. Table 2 shows the best two designs, but for the total performance, G15N11S40 is recommended. R7N08N65 has rectangular blades, a solidity of 0.7, normal blades, 8 blades, and tip gab of 0.65 mm. The G15N11S40 has 1.5 solidity, 11 blades, and the axial spacing between rotor and guide vane equal to 40 mm.

The effects of unsteady flow conditions on the performance of a monoplane Wells turbine without guide vanes during a field experiment on a OWC device are described in [23, 24]. The torque coefficient shows a hysteretic mechanism characterized by a counter-clock-wise loop that appears with high frequency oscillations. A dynamic stall phenomenon appears with oscillations of very large amplitude, independently from the frequency. A computational model has been used in [20] to study the performance and aerodynamics of the turbine, quantitatively and qualitatively. In addition, it is used to study the flow coefficient, turbine stalls and the appropriate inlet velocity profile. It is found from the computed results that the wakes behind the turbine blades (NACA0021) merge rigorously in the portion of Radius ratio = 0.45:1.0, which leads the turbine to stall. The tip gab leakage flow is considerably higher in the trailing edge portion. However, as the flow coefficient increases, leakage flow region advances towards the leading edge, causing a large mass flow of air to leak through the gap. A comparison between numerical and experimental investigations is conducted in [25] for studying uniform tip gab ratio. Regarding turbine efficiency, it is found that the peak efficiency of the turbine decreases, and shifts towards a higher flow coefficient as the tip gab to chord length ratio increases, while the stall margin becomes wider.

The entropy generation, due to viscous dissipation, was investigated by [26, 27] for Wells turbine airfoil sections. The efficiency for four different airfoils in compression cycle is higher than suction cycle at 2 º angle of attack. But when the angle of attack increases, the efficiency for suction cycle increases also more than the compression one. This study suggested that a possible existence of critical Reynolds number at which viscous irreversibilities takes minimum values. Exergy analysis [28] is performed using the numerical simulation for steady state biplane Wells

turbines [29] where the upstream turbine has a design point second law efficiency higher than the downstream turbine second law efficiency by 21.6%. The total entropy generation, due to viscous dissipation, for suggested design for Wells turbine with variable chord was compare with Wells turbine with constant chord in [30]. The detailed results demonstrate 26.02 % average decrease in total entropy generation throughout the full operating range. Recent studies proved that entropy generation within various wave energy extracting systems plays a significant role in determining the overall efficiency of the system [31, 32]. Thus, researchers must take into account the entropy analysis for the Wells turbine while investigating the wave energy extracting performance. Since, it has shown very promising result in many applications, such as wind turbine in [33-38] and gas turbine in [39-41].

One of the most popular methods that have been used to decrease flow separation around the aerofoil section and delay the stall is the flow control method [42-47]. Different studies have been conducted on flow control techniques. The first scientist who employed boundary layer suction on a cylindrical surface to delay boundary layer separation was Prandtl in 1904 [48]. The earliest known experimental works on boundary layer suction for airfoil and wings were conducted in the late 1930 and the 1940 [49-51]. The idea of passive suction is to use a passive porous surface [52] [53] to mitigate the local pressure gradients and obviate separation to reduce drag. Huang et al. [54] studied the suction and blowing flow control techniques on a NACA0012 airfoil. It can be concluded that perpendicular suction at the leading edge increased lift coefficient more than other suction situations. The tangential blowing at downstream locations was found to lead to the maximum increase in the lift coefficient value. The study in [55] provide an excellent review of the various periodic excitation methods, mainly steady suction and blowing. This review gives a detailed discussion of the mechanism and also the recent developments in the field. Previous reviews that provide a detailed discussion of the subject include [56-60]. The CFD method has been used to investigate boundary layer control [61-63] such as the effects of blowing and suction jets on the aerodynamic performance of airfoils.

One of the best locations to apply the OWC system with Wells turbine is the northern coast of Egypt [64]. Where, the most energetic coast of the Southern Mediterranean Basin is the Egyptian coast, lying between the Nile Delta and the Libyan borders with a potential of above 3.35 kW/m wave power in summer and 6.8 kW/m in winter [65, 66] and the wave energy of about 36003 kWh/m. Wave energy potential of the Eastern Mediterranean Sea Basin was assessed and

characterized. Wave fields obtained from 3rd generation spectral wave model for years 1994-2009 by using wind data from European Center for Medium-Range Weather Forecasts (ECMWF) were used in order to calculate the wave powers. Wave model was calibrated using the wave measurements conducted at three different stations. Wave model simulated the wave characteristics such as significant wave heights and mean wave periods with high accuracy. Wave power atlas was generated based on 15-year time-averaged wave data. Also wave power roses and distribution tables in means of periods and heights for different regions were presented [67]. The most energetic sea states have significant wave heights between 1 and 4 m and wave energy periods between 4 and 8 second. The regions with increased wave energy potential are mainly the western and southern coastlines of Cyprus Island, the sea area of Lebanon and Israel, as well as the coastline of Egypt, especially around Alexandria. The significant differences between the sea in Egypt and other seas are that the sea wave in Egypt is relatively low but also stable. Hence, the potential wave energy can be revealed and exploited. Otherwise, sea states with the wave heights greater than 5 m are not very important for the annual energy [68] as they contribute little to the annual energy. But they need to be considered in design and selection of wave energy converters. Although Eastern Mediterranean and Aegean Sea Basins can be regarded as low potential areas in terms of wave energy, future developments in the wave energy converter technologies can make gathering energy economically viable.

Current researchers are only investigating the aerofoil with the passive flow control methods, such as the suction and blowing slot under steady (non-sinusoidal) flow. Therefore, the objective of the present work is to investigate the passive flow control methods (e.g. the suction and blowing slot) which affect the entropy generation behavior under sinusoidal flow. While improving the generated torque coefficient on the aerofoil section with the attached slot, it is equally important to accurately model the effect on the entropy generation and the second law efficiency. Therefore, it is essential that to investigate and define the optimum parameters (e.g. slots number, locations, and angle) for single and multi-slots based on the first and second law analysis. Then, the turbine blade with optimum suction slots number and location was investigated using the oscillating water system based on the real data from the northern coast of Egypt. Where, the present work recommends Wells turbine as a suitable choice for the Egyptian coasts due to its simple and efficient operation under low input air flow. Furthermore, in view of the previous research in the section of the connections with other turbines, it can be concluded that the efficiency of Wells

turbine is higher than that of the other turbines when the flow coefficient is less than the stall point. But after the stall point of Wells turbine, the efficiency of the others turbine (such as impulse turbine) is considerably higher than that of Wells turbine. In other words, Wells turbine can extract power at a low air flow rate, when other turbines would be inefficient. To the best of this author's knowledge, to date no study exists which define the optimum location and number for multi-slots attached to the aerofoil under sinusoidal flow inlet velocity based on the first and second law analysis. Furthermore, to date no specific unsteady CFD study of the multi-slots effect with sinusoidal flow on the entropy generation rate has been performed for Wells turbine.

2. Mathematical Formulations and Numerical Methodology

In order to solve the governing equations of Large Eddy Simulation (LES), the time-dependent Navier-Stokes terms are filtered. This filtering process aims to eliminate eddies that have scale smaller than the filter width or computational mesh spacing. Therefore, the resulting filtered equations govern the dynamics of large eddies. A filtered variable (denoted by an over-bar) could be expressed as [69]:

$$\overline{\phi}(x) = \int_D \phi(x')G(x,x')dx' \quad (1)$$

where D represents the fluid domain, and G represents the filter function that determines the scale of the resolved eddies. The unresolved part of a quantity ϕ is defined by:

$$\phi' = \phi - \bar{\phi} \quad (2)$$

And the filtered fluctuations are not zero:

$$\overline{\phi'} \neq 0 \quad (3)$$

In FLUENT, the filtering operation is implicitly provided in the finite-volume discretization [1]:

$$\overline{\phi}(x) = \frac{1}{V}\int_V \phi(x')dx', \ \ x' \in V \quad (4)$$

where V is the volume of the control volume. The filter function, G (x, x'), is expressed as

$$G(x,\ x') = \begin{cases} 1/V & for \ \ x' \in V \\ 0 & otherwise \end{cases} \quad (5)$$

While this LES model is treating incompressible flows, not necessarily constant-density flows are assumed. Filtering the incompressible Navier-Stokes terms, one obtains [70]

$$\frac{\partial \rho}{\partial t} + \frac{\partial \rho \overline{u}_i}{\partial x_i} = 0 \quad (6)$$

$$\frac{\partial}{\partial t}(\rho\overline{u}_i) + \frac{\partial}{\partial x_j}(\rho\overline{u}_i\overline{u}_j) = \frac{\partial}{\partial x_j}\left(\mu\frac{\partial\overline{u}_i}{\partial x_j}\right) - \frac{\partial\overline{\rho}}{\partial x_i} - \frac{\partial\tau_{ij}}{\partial x_j} \quad (7)$$

Where τ_{ij} is the sub-grid-scale stress obtained as

$$\tau_{ij} = \rho\overline{u_i u_j} - \rho\overline{u_i}\ \overline{u_j} \quad (8)$$

Since these sub-grid-scale stresses are unknown, to obtain them an extra modeling step is required. The majority of the eddy viscosity models are of the following form [71]:

$$\tau_{ij} - \frac{1}{3}\tau_{kk}\sigma_{ij} = -2\mu_t\overline{S}_{ij} \quad (9)$$

Where $\overline{S}_{ij}$ is the rate-of-strain tensor which obtained by:

$$\overline{S}_{ij} = \frac{1}{2}\left(\frac{\partial\overline{u}_i}{\partial x_j} + \frac{\partial\overline{u}_j}{\partial x_i}\right) \quad (10)$$

and μ_t is the sub-grid-scale turbulent viscosity. The most basic of sub-grid-scale models for "Smagorinsky-Lilly model" was proposed by Smagorinsky [72, 73] and further developed by Lilly [74]. In, the eddy viscosity is modeled by Smagorinsky-Lilly model as:

$$\mu_t = \rho L_s^2 \left|\overline{S}\right| \quad (11)$$

where L_s is the mixing length for sub-grid-scale models and $\left|\overline{S}\right| = \sqrt{2\overline{S}_{ij}\overline{S}_{ij}}$. The L_s is calculated as follows:

$$L_s = \min(kd, C_s V^{1/3}) \quad (12)$$

Where C_s is the Smagorinsky constant, $k = 0.42$, d is the distance to the closest wall, and V is the volume of the computational cell. Lilly derived a value of 0.23 for C_s from homogeneous isotropic turbulence. However, this value was found to cause excessive damping of large-scale fluctuations in the presence of mean shear or in transitional flows. A dynamic SGS model was not particularly necessary in the LES models due to the turbulence flow at all domain, therefore, C_s= 0.1 has been found to yield the best results for a wide range of flows [1, 75, 76].

For the first law of thermodynamics, the lift and drag coefficient C_L and C_D could be calculated from the post processing software. A single value for the torque coefficient for each angle of attack was calculated using average values for lift and drag coefficients. Thus, the torque coefficient can be calculated as [77]:

$$C_T = (C_L\ sin\,\alpha - C_D\ \cos\alpha) \quad (13)$$

The flow coefficient, $\bar{\phi}$, relating tangential and axial velocties of the rotor is difined as

$$\bar{\phi} = \frac{V_a}{\omega * R_m} \quad (14)$$

where the angle of attack, α, equals to

$$\alpha = tan^{-1} \frac{V_a}{\omega R_m} \quad (15)$$

and the torque as:

$$Torque = \frac{1}{2}\rho\left(V_a{}^2 + (\omega R_m)^2\right) AR_m C_T \quad (16)$$

The first law of thermodynamics efficiency (η_F) is defined as:

$$\eta_F = \frac{Torque * \omega}{\Delta P * Q} \quad (17)$$

According to the second law of thermodynamics, the net-work transfer rate $\dot{W}$ as [78]:

$$\dot{W} = W_{rev} - T_o S_{gen} \quad (18)$$

Which, it has been known in engineering as the Gouy–Stodola theorem [79].

It is possible to express the irreversible entropy generation in terms of the derivatives of local flow quantities in the absence of phase changes and chemical reactions. The two dissipative mechanisms in viscous flow are the strain-originated dissipation and the thermal dissipation which correspond to a viscous and a thermal entropy generation respectively [80]. Thus, it can be expressed as,

$$S_{gen} = S_V + S_{th} \quad (19)$$

The case in hand represents an incompressible isothermal flow, where the thermal dissipation term vanishes. Therefore, the local viscous irreversibilities can be expressed as [26, 27]:

$$S_V = \frac{\mu}{T_o}\phi \quad (20)$$

where ϕ is the viscous dissipation term, that is expressed in two dimensional Cartesian coordinates as [80]:

$$\phi = 2\left[\left(\frac{\partial u}{\partial x}\right)^2 + \left(\frac{\partial v}{\partial y}\right)^2\right] + \left(\frac{\partial u}{\partial y} + \frac{\partial v}{\partial x}\right)^2 \quad (21)$$

Equation 20 and 21 were used to create the custom field function file, which is used to calculate the local entropy form the FLUENT software. Then, the global entropy generation rate is hence expressed as:

$$S_G = \iint_{xy} S_V \, dydx \tag{22}$$

Which is also calculated from the FLUENT software by integrating the global value,
Equation (23) defines the exergy value as:

$$Exergy = KE + S_G \tag{23}$$

Finely the second law efficiency is defined as [33]:

$$\eta_S = \frac{KE}{Exergy} \tag{24}$$

Where $KE = \frac{1}{2} V^2$

From the above equations, it can be concluded that the torque coefficient is related to the first law efficiency , where the increase in torque coefficient leads to an increase in the first law efficiency. Moreover, the global entropy generation rate is related to the second law efficiency, where the decrease in the global entropy generation rate leads to an increase in the second law efficiency.

3. CFD Approach

The CFD verification and validation result for such models used in this work is presented. Also, this section is contains a description of the turbulence models used in stall condition, an expression of the discretization methods employed and the boundary conditions for this work

3.1 Computational model and boundary conditions

2D numerical simulations model for NACA0015 airfoil were conducted and their results were validated against experimental measurements. Both unsteady flow with non-oscillating velocity, as well as, unsteady flow with sinusoidal inlet velocity were investigated. A Cartesian structured mesh was generated using (GAMBIT V-2.4.6) software for discretizing the computational domain. The application matches the Green-Gauss cell based evaluation method for the gradient terms used in the solver (ANSYS FLUENT V-14.5). For these cases it was found that the second

order upwind [81] interpolation scheme yields approximately similar results to those yielded by third order MUSCL scheme in the present situation. Moreover, sometimes the third order MUSCL scheme produces high oscillatory residual during the solution. Therefore, the second order upwind [81] interpolation scheme was used in this study. The Quad-Pave meshing scheme (Structured Grid) was used in this study. It was also found that the solution reaches convergence when the scaled residuals approaches 1×10^{-5}. At this residuals limit, the flow field variables preserve constant values with the application of consecutive iterations.

The axial flow entering Wells turbine was modelled as: 1) a non-oscillating velocity and 2) a sinusoidal wave in this simulation. Therefore, inlet boundary conditions were time dependent. In order to apply the inlet sinusoidal wave boundary condition, inlet velocity with periodic function was generated based on Equation (25). This periodic function was introduced as a user defined function in FLUENT. According to the literature, this equation is used for modeling a sinusoidal wave inlet flow with a non-zero mean velocity over various objects [82, 83].

$$V_a = V_o + V_{am}\ sin\ (\sin 2\pi f t_{sin}) \quad (25)$$

Where, the V_o and V_{am} are equal to 0.04 and 2.88 m/s respectively, t_{sin} is the sinusoidal wave time period, and f is the wave frequency. Based on the conducted literature survey, t_{sin} for a single period was taken as 6 seconds (f equal to 0.167 Hz) in this simulation [75, 76, 84, 85]. In order to satisfy CFL (Courant Friedrichs Lewy) condition equal to 1, the time step was set as 0.000296721 second [86]. For the Egyptian coasts boundary condition, the most energetic sea states have wave energy periods between 4 and 8 seconds. Therefore, the time period t_{sin} was taken as 4, 6, and 8 seconds (f equal to 0.25, 0.167 and 1.25 Hz) and is set as one period in this simulation, considering the real data from the Egyptian coasts. The sinusoidal wave condition create various Reynolds number up to 2×10^4 according to the reference [87]. Figure 1 shows the dimensions of the computational domain and the position of the airfoil.

3.2 Grid-independent solution

Several computational grids were tested to ensure a grid-independent solution. The structured grids (Quad-Pave meshing scheme) used in unsteady flow with non-oscillating velocity. The

pressure coefficient distribution on the upper and lower surfaces of the NACA0012 aerofoil was computed by the four grids ranging from 112603 up to 446889 cells. Grid 4 (with 446889 cells and 1 x 10^{-6} for the first cell with growth rate equal to 1.01) required more time than grid 3, yielding similar results for pressure coefficient values. Therefore, grid 3 (with 312951cells and 1 x 10^{-5} for the first cell with growth rate equal to 1.012) was chosen to conduct the analysis presented hereafter, more details about grid sensitivity results can be found in [26, 64].

3.3 Validation of the CFD model

According to literature [70, 88-95], Large Eddy Simulation model excels in predicting flows over airfoil in stall condition. Although LES is a 3D model by definition, there have been numerous successful attempts to use it in 2D applications [6, 64]. In this study, two sets of experimental data were used to validate the numerical model from references. First experimental data [87, 96, 97] was used to simulate and validate the results at stall condition. The first validation case involved the investigation of Wells turbine prototype with the following parameters:

- NACA0015 blade profile
- Hub radius = 101 mm;
- Tip radius = 155 mm;
- Chord length = 74 mm;
- Number of blades = 7;
- Hub-to-tip ratio = 0.65;
- Solidity = 0.64;
- The uncertainty in the measurements = 5%

Second experimental data [83] is adopted to validate the unsteady sinusoidal wave inlet velocity. The second experimental data involved the investigation of unsteady forces (F_D) acting on a square cylinder in oscillating flow with nonzero mean velocity. The oscillating air flows are generated by a unique AC servomotor wind tunnel. The generated velocity histories are almost exact sinusoidal waves.

For unsteady flow with non-oscillating and oscillating velocity, it was validated in [6], where, a comparison between the measured torque coefficient from reference [87, 96, 97] and calculated

torque coefficient from CFD results at Reynolds number of 2×10^4. This comparison yields a very good agreement. It can be noted that approximately the same stall condition value of the experimental reference was recorded by the computational model. Furthermore, for an unsteady flow with sinusoidal inlet velocity, Figure 2 shows a good agreement between measured drag force from reference [83] and predicted drag force from CFD at two different frequencies (2 Hz and 1 Hz). It can be shown from Figure 2 that the computational model has almost the same behavior of oscillating flow condition as the reference. Table 3 lists the error percentages for each frequency.

4. Analysis and Discussion of Results

A multi-suction slot with a certain diameter (D_{ss}) equal to 0.1% [6] from the blade chord at various locations from the leading edge was created, with a shape of NACA0015 with stall angle equal to 13.6 º and Reynolds number equal to 2×10^5 from reference [87, 96, 97], see Figure 3. The locations for the suction slots were changed in order to obtain an optimum value of C_T. The test cases investigated were under unsteady flow with non-oscillating velocity at the first to indicate to the best locations and then take the best cases to investigate under sinusoidal wave condition to decide which one has the highest C_T and which one has the lowest S_G. The sinusoidal wave inlet flow boundary condition is having the same specifications as that in the section 3.1 and equation (25). Finally, a comparative analysis was made based on conditions relevant to northern coast of Egypt with different sinusoidal wave frequencies (f equal to 0.25, 0.167 and 1.25 Hz).

4.1 Multi suction slots (Two, Three and Four)

The two suction slots were investigated by making the first suction slots as a reference (L_{Rss}) and changing the location (x axis direction) of the second suction slots (L_{ss}) by pitch distance (P_{ss}) equal to 0.05 at each trial. Considering that, the minimum distance between the two suction slots (ΔP_{ss}) was equal to 0.05.

Table 4 provides the details about all two suction slots trial with $P_{ss}$and ΔP_{ss} equals to 0.05 to improve the torque coefficient at the stall angle 13.6 º. It can be noted that the L_{Rss} equal to 40% and L_{ss} equal to 45% gives a higher torque coefficient than others, where the torque coefficient increases about 82% higher than the aerofoil without suction slot at the stall angle. Therefore, to

get more improvement in the torque coefficient, the value of P_{ss} and ΔP_{ss} was changes to 0.01 around the L_{ss} 40% and L_{ss} 45%. It can be concluded that two suction slots at L_{Rss} 40% and L_{ss} 44% with P_{ss} equal to 0.01 give a higher torque coefficient than others by 84% at the stall angle in Figure 4 A). On the other hand, two suction slots at L_{Rss} 45% and L_{ss} 49% give also a higher torque coefficient than others by 84% at the stall angle from Figure 4 B).

From Table 4 and Figure 4, it can be noted that the three optimum locations for two suction slots were L_{ss}40% and 45% with P_{ss} equal to 0.05, in addition to L_{ss} 40% and 44% and L_{ss} 45% and 49% with P_{ss} equal to 0.01. Table 5 demonstrates the effect of the three optimum locations for two suction slots on the torque coefficient at different angles. It can be noted that the two suction slots at L_{ss} 40% and 45% improve the torque coefficient before the stall by 37.2% and after the stall by 95.5%. Also, the two suction slots at L_{ss} 40% and 44% improve the torque coefficient before the stall by 33.5% and after the stall by 97.5%. Finally, the two suction slots at L_{ss} 45% and 49% improve the torque coefficient before the stall by 36.7% and after the stall by 99%.

The suction slots have a negative effect on the entropy generation, where the global entropy generation rate increases at all angles by 24% before the stall and 23% after the stall due to suction slots at (L_{ss}40% and 45%). Where, the 11.3 º angle of attack (before the stall) has the highest difference in global entropy generation rate by 38%. On the other hand, 11.7 º angle of attack (before the stall) has the lowest difference in global entropy generation rate by 13 % due to suction slots at Figure 5 A). Furthermore, the suction slots at (L_{ss}40% and 44%) cause increase in the global entropy generation rate value as average for all angles by 21% before the stall and 26% after the stall at Figure 5 B). The 10.1 º angle of attack (before the stall) has the lowest difference in global entropy generation rate by 14% due to suction slots and, the 14.4 º angle of attack (after the stall) has the highest difference by 29 %. Finally, for suction slots at (L_{ss}45% and 49%) at Figure 5 C), the global entropy generation rate increases as average in all angles by 21% before the stall and 22% after the stall. Where, the 10.6 º (before the stall) has the highest difference in global entropy generation rate by 44% and, the 12.3 º (before the stall) has the lowest by 11 % due to suction slots. This phenomenon suggests that the change in velocity gradient due to the suction slot has a direct impact on the entropy generation.

A third suction slot by P_{ss} equal to 0.05 was added to all aerofoils with two suction slots that have higher than 70% improvement in the torque coefficient at the stall angle 13.6 º. Table 6 provides all three suction slots trial with $P_{ss}$and ΔP_{ss} equal to 0.05 to improvement the torque coefficient at the stall angle (13.6 º). It can be noted that the L_{Rss} equal to 40% - 55% and L_{ss} equal to 90% gives a higher torque coefficient than others, where the torque coefficient increases about 94% higher than the aerofoil without suction slot. Therefore, to get more improvement in the torque coefficient, the value of $P_{ss}$and ΔP_{ss} was changes to 0.01 around the L_{ss}40%, 55% and 90%. From Table 7, it can be noted that no improvement on the torque coefficient by change P_{ss} from 0.05 to 0.01 around the L_{ss}40%, 55% and 90%.

It is clearly noted that the three suction slots at (L_{ss}40%, 55% and 90%) improve the torque coefficient before the stall by 35.2% and after the stall by 97%, see Figure 6 A). On the other hand, the global entropy generation rate increases for all angles by 29% before the stall and 25% after the stall as average value at Figure 6 B). Where, the 10.1 º angle of attack (before the stall) has the highest difference in global entropy generation rate by 36% due to suction slots at (L_{ss} 40%, 55% and 90%), and the 11.7 (before the stall) and 13.6 (after the stall) º have the lowest difference by 23 %.

A fourth suction slot with P_{ss} equal to 0.05 was added to all aerofoils with three suction slots that have higher than 80% improvement in the torque coefficient at the stall angle (13.6) º. Table 8 shows the effect of four suction slots on the torque coefficient at the stall angle (13.6 º) with $P_{ss}$and ΔP_{ss} equal to 0.05 to improvement the torque coefficient. The L_{Rss} equal to 40% - 45% - 55% and L_{ss} equal to 60% gives a higher improvement in the torque coefficient by 92%. As in two and three suction slots, the value of $P_{ss}$and ΔP_{ss} changes to 0.01 around the L_{ss}40%, 45%, 55% and 60% to get more improvement in the torque coefficient. From Table 9, it can be noted that the L_{ss}40%, 45%, 55% and 60% give highest improvement on the torque coefficient with P_{ss} equal to 0.01. The four suction slots (L_{ss}40%, 45%, 55% and 60%) improve the torque coefficient before the stall by 35.8% and after the stall by 99%, see Figure 7 A). Otherwise, the global entropy generation rate increases by 29% before the stall and 26% after the stall at Figure 7 B).Where, the 10.1 º has the lowest difference in global entropy generation rate by 16% and, the 10.6 º has the highest difference by 52 %. The path line coloured by the mean velocity magnitude around the NACA0015 without and with slots at the stall angle 13.6 º was presented at Figure 8. The slots

effect was very cleared on the separation layers at the trailing edge area and it extends to the area beyond the trailing edge which, leads to delay the stall. Therefore, the NACA0015 with suction slots and Reynolds number equal to 2×10^5 not have the stall condition at 13.6 º. This improvement can be achieved by two, three or four slots at different location. Where, each case of them has different behaviour.

The low pressure areas, at the trailing edge of the NACA0015 without slots, were caused the separation layer. On the other hand, the suction slots affect directly on these areas and decrease from its value and this leads to decrease the separation layers (Figure 9). The difference between the upper and lower surface was decreased by the suction slots and this leads to decrease from the disturbance and the separation layers (Figure 10). The pressure distribution at the upper and lower surface was depending on the number and location of the slots. Therefore, the two, three and four slots were investigated under sinusoidal wave condition in next section.

4.2 Optimum location for multi-suction slots based on first law analysis

From the previous section, it was noted that there are five scenarios for the suction slots location, which gives higher torque coefficient at the stall regime:

1- Two Suction Slots (L_{ss}40% and 45%) with P_{ss} = 0.05
2- Two Suction Slots (L_{ss}40% and 44%) with P_{ss} = 0.01
3- Two Suction Slots (L_{ss}45% and 49%) with P_{ss} = 0.01
4- Three Suction Slots (L_{ss}40%, 55% and 90%) with P_{ss} = 0.05
5- Four Suction Slots (L_{ss}40%,45%, 55%, and 60%) with P_{ss} = 0.05

In this section, the optimum locations for multi-suction slots based on the torque coefficient were determined under sinusoidal wave condition. Figure 11 compares the torque coefficients for the two suction slots aerofoil at different locations (L_{ss}40% and 45%), (L_{ss}40% and 44%) and (L_{ss}45% and 49%). Figure 11 A) illustrates the hysteretic behaviour due to the reciprocating flow which shows a delay in the stall regime and an improvement in the torque coefficient. The two suction slots aerofoil with L_{ss} of 40% and 44% has a higher improvement of torque coefficient than that with L_{ss} of 40% and 45% by 6.3% before the stall and 1.5 % after the stall. Moreover, the former aerofoil also has a higher torque coefficient than that with L_{ss} of 45% and 49% by 1% before the stall and 2.5 % after the stall (Figure 11 B).

Figure 12 shows the effect of adding three suction slots at (L_{ss}40%, 55% and 90%) and four suction slots at (L_{ss}40%, 45%, 55%, and 60%) under sinusoidal flow condition on the hysteretic behaviour. From this Figure, it can be noted that in both cases a delay in the stall regime occurred. In addition, the torque coefficient was improved by 26.7% before the stall and 51 % after the stall due to the addition of three suction slots (Figure 12 A). However, the addition of four suction slots resulted in torque coefficient improvement by 25.7% before the stall and 40.5% after the stall (Figure 12 B).

From Figure 13, it is clearly noted that adding three suction slots at (L_{ss}40%, 55% and 90%) provided the highest improvement of torque coefficient, from both the instantaneous and average value, compared to all the scenarios that were mentioned in this section. By comparing this aerofoil against the two suction slots aerofoil with optimum locations (L_{ss}40% and 44%), an improvement of torque coefficient of 2.7% before the stall and 22.5% after the stall was observed. Moreover, by comparing the same aerofoil against the four suction slots aerofoil (L_{ss}40%, 45%, 55%, and 60%), an improvement of torque coefficient of 1% before the stall and 10.5% after the stall was observed.

The path-line coloured by mean velocity magnitude highlights the improvement effect of adding a suction slot on the separation layers in Figures 14, 15 and 16. The effect of adding a suction slot on the separation layers at the trailing edge region in Figure 14 (acceleration flow) was small compared with Figures 15 and 16. Where, the separation layers at the area around the trailing edge increased especially at the deceleration flow in the second half of the compression cycle (Figure 16). Furthermore, it can be noted that the low pressure areas around the trailing edge decrease due to the slots addition from Figures 17 and 18. The pressure difference between the lower and upper surfaces was decreased as a result of adding the slots. Therefore, the disturbances in the path line at the trailing edge area and the area extended beyond it was decreased. This leads to delay the stall and improve the torque coefficient.

Figure 19 shows the effect of adding three suction slots on the boundary layer separation before and after the stall condition via the mean velocity magnitude path-lines. It can be noted that the improvement effect of adding suction slot on separation layers increased in stall regime for both 13.6 and 14.4 º. The pressure distributions around the aerofoil and at the upper and lower surfaces

for different angles of attack were shown in Figures 20 and 21. Where, the lift column is for the NACA0015 without slots and the right column is for the NACA0015 with three slots at L_{ss}40%, 55% and 90% with maximum velocity equal to 2.92 m/s. The addition of three slots affects directly the low pressure zones that appear around the trailing edge area and the upper surface of the aerofoil. Where, this low pressure zones were the main reason for the separation layers to be formed. For all angles, the aerofoil with three slots showed an improvement in the pressure distribution and decreased the separation layers especially for the stall angle of 14.4 º in Figure 19 I) and J).

4.3 EGM method

The numerical simulations were used to obtain local entropy viscosity predictions from the different five scenarios for the locations of suction slots. Figures 22 and 23 highlight the comparison between the (L_{ss}40% and 45%), (L_{ss}40% and 44%), (L_{ss}45% and 49%), (L_{ss}40%, 55% and 90%) and (L_{ss}40%, 45%, 55%, and 60%). The comparison was provided as an average value for the compression cycle with different angles of attack. From Figure 22 A) it can be noted that the minimum value for the global entropy generation rate occurs with (L_{ss}45% and 49%) by 20.24% increase in S_G before the stall. On the other hand, the minimum value for the global entropy generation rate occurs with (L_{ss}40% and 45%) by 14.54% increase in S_G after the stall; see Figure 22 B). Furthermore, the two suction slots (L_{ss}40% and 45%) give minimum S_G as an average value for the compression cycle before and after the stall by 20.5% increase in S_G value.

From Figure 23 it can be concluded that the (L_{ss}45% and 49%) gives the maximum value of second law efficiency by 0.38% before the stall, and, the (L_{ss}40% and 45%) gives the maximum value after the stall by 1.19%. Furthermore, the two suction slots (L_{ss}40% and 45%) give maximum value for the second law efficiency as an average value for the compression cycle before and after the stall by 0.72%. The increases in S_G (Figure 22) leads to decrease in second law efficiency in some cases than that without suction slots, such as the two suction slots at $L_{ss} = 40\%$ and $L_{ss} = 44\%$ before the stall which the second law efficiency decreased by (0.01%), and three suction slots at $L_{ss} = 40\%$, $L_{ss} = 55\%$ and $L_{ss} = 90\%$ after the stall which the second law efficiency decreased by (0.61%). There were no significant changes in both the global entropy

generation rate values and the second law efficiency due to the different slots number and location.

The contours of global entropy generation rate around the NACA0015 at the instantaneous velocity 1.8 m/s for the accelerating (Figure 24) and decelerating flow (Figure 26) in addition 2.92 m/s (Figure 25) were represented. Where, the 2.92 m/s was the maximum velocity which create the peak Reynolds number (2×10^5), and 1.8 m/s is approximately at the middle to compare between the accelerating and decelerating flow. It can be shown that the suction slots have a negative effect on the entropy generation, where the global entropy generation rate increases at the three stages, accelerating flow, maximum velocity and decelerating flow at 13.6 º. The two-suction slots at (L_{ss}40% and 45%) and (L_{ss}45% and 49%) have the lowest difference in global entropy generation rate by 32% at the accelerating flow in Figure 24. Otherwise, the three-suction slots at (L_{ss}40%, 55% and 90%) have the highest difference in global entropy generation rate by 44 % at the same Figure. However, the global entropy generation rate has lowest difference due to suction slots at the maximum velocity by 28% with the two-suction slots at (L_{ss}40% and 45%). Also, the highest value occurs due to the two suction slots at (L_{ss}40% and 44%) by 35% in Figure 25.

From Figure 26 it can be noted that the two suction slots at (L_{ss}40% and 45%) has the lowest difference in global entropy generation rate by 37% and the highest value occurs due to the three suction slots at (L_{ss}40%, 55% and 90%) by 53% at the decelerating flow. Finally, the global entropy generation rate around the NACA0015 without and with suction slots have the highest value at the maximum velocity and the lowest value at the accelerating flow as a general. From Figures 14, 15, 16, and 19 it can be noted that the attached multi-slots to the aerofoil lead to increase in velocity magnitude around the aerofoil, furthermore, it lead also to increase in the entropy generation in Figures 24, 25, and 26. Where, the entropy value depends on the velocity gradient see equation (21).

4.4 Comparative analysis based on conditions relevant to northern coast of Egypt

From the previous section, it can be concluded that the three-suction slots (L_{ss}40%, 55% and 90%) give maximum C_T and the two-suction slots (L_{ss}40% and 45%) have the lowest S_G from the

five scenarios, which give higher torque coefficient. Therefore, these two scenarios were investigated using the oscillating water system based on the real data from the site with different time periods and frequencies (f equal to 0.25, 0.167 and 1.25 Hz). The hysteretic behaviour due to the reciprocating flow and the total average torque coefficient during the cycle for aerofoil with suction slots at different time periods were shown in Figure 27. It can be concluded that the aerofoil with three-suction slots (L_{ss}40%, 55% and 90%) give higher C_T than that with two-suction slots (L_{ss}40% and 45%) at 4, 6 and 8 second time period. Also, the increase in time period led to a decrease in the total average torque coefficient in general. At the time period equal to 4 second, the aerofoil with two-suction slots (L_{ss}40% and 45%) has an average torque coefficient after the stall less than the aerofoil without suction slots by 8.5%. Furthermore, the aerofoil with two suction slots (L_{ss}40% and 45%) with 8 second time period has improvement in the total average torque coefficient before the stall by 17% and after the stall by 8%.

Figures 28 and 29 show the instantaneous torque coefficient in addition to average torque coefficient at the accelerating and decelerating cycle for aerofoil with two-suction slots and with three-suction slots. These values were at angle of attack of 13.6 º at different time periods (4 sec, 6 sec and 8 sec). It can be seen that the improvement in the torque coefficient has the lowest value at the cycle with time period equal to 4 second. Furthermore, the torque coefficient value and improvement in the torque coefficient at decelerating flow are always higher than that at accelerating flow.

The total average torque coefficients during the compression cycle for different angles of attack were shown in Figure 30. It can be observed that for all angles, the suction slot increases the torque coefficient except at the 14.4 º Figure 30 E), where the torque coefficient for the aerofoil with two-suction slots (L_{ss}40% and 45%) was lower than that without suction slots by 24% at time period 4 second. Also, the torque coefficient at time period 8 second for the aerofoil with two-suction slots (L_{ss}40% and 45%) was same for that without suction slots. The aerofoil with three-suction slots (L_{ss}40%, 55% and 90%) mostly has a higher torque coefficient than that of the two-suction slots (L_{ss}40% and 45%) at different time period.

Tables 10, 11 and 12 show the comparison between the global entropy generation rate before and after the stall for the aerofoil with two-suction slots (L_{ss}40% and 45%) and with three-suction

slots (L_{ss}40%, 55% and 90%) at different time periods (4 sec, 6 sec and 8 sec). There were no significant changes in the global entropy generation rate values due to the different time periods. As an average for all time period, the aerofoil with two-suction slots (L_{ss}40% and 45%) has a lower difference in S_G before and after the stall than the aerofoil with three- suction slots (L_{ss}40%, 55% and 90%).

Suction slots have a negative effect on both the entropy behaviour and the second law efficiency. Therefore, most of cases at Figure 31 have lower second law efficiency for aerofoils with slots than the aerofoils without slots. As it noted in the entropy behaviour, there were also no significant changes in the second law efficiency value due to the different slots number and location. However, the second low efficiency at 14.4 º for the aerofoil with two suction slots (L_{ss}40% and 45%) was the highest value at 4, 6 and 8 second by 1%, 2% and 3% respectively, Figure 31 E). The wave cycle with 8 second has the highest value of the second law efficiency as a general. On the other hand, the wave cycle with 6 second has the lowest value. The aerofoil with two-suction slots (L_{ss}40% and 45%) always has higher second law efficiency than that with three-suction slots (L_{ss}40%, 55% and 90%) at the different time periods.

The flow structures over the NACA0015 aerofoil in oscillating flow was shown in Figure 32 at angle of attack equal to 12.3 º (before the stall) and 14.4 º (after the stall) in Figure 33. The improvement effect of suction slot on flow structures was clear when comparing the NACA0015 without and with suction slots, especially in the separated layer regime at the end of aerofoil, which leads to an improvement in the separation regime.

5. Conclusions

More than 450 cases were solved to determine optimum location for multi suction slots based on the first and second law of thermodynamics. They aimed to investigate the effect of aerofoil with those optimum parameters on the entropy generation due to viscous dissipation as well as the torque coefficient and stall condition. After that, the comparative analysis based on real data relevant to northern coast of Egypt was applied using the aerofoil with optimum suction slot parameters.

The modeling results show that the optimum locations for two-suction slots aerofoil (L_{ss} of 40% and 44%), for three-suction slots aerofoil (L_{ss} of 40%, 55% and 90%), and for four-suction slots aerofoil (L_{ss} of 40%, 45%, 55%, and 60%). The three-suction slots aerofoil with L_{ss} of 40%, 55% and 90% gives the highest torque coefficient with 26.7% before the stall and 51% after the stall when compared to the aerofoil without suction slots. On the other hand, the two-suction slots aerofoil with L_{ss} of 40% and 45% gives the highest second law efficiency by 0.72% compared to the aerofoil without suction slots. The aerofoils with optimum locations for multi-suction slots under conditions relevant to northern coast of Egypt with different wave frequencies were investigated. For NACA0015, adding three-suction slots at optimum locations (L_{ss} of 40%, 55% and 90%) mostly gives a torque coefficient higher than that of adding two suction slots at optimum locations (L_{ss} of 40% and 45%) for different t_{sin} (4, 6 and 8 second). However, adding two-suction slots at optimum locations (L_{ss} of 40% and 45%) always gives a second law efficiency higher than that of adding three-suction slots at optimum locations (L_{ss} of 40%, 55% and 90%) for different t_{sin} (4, 6 and 8 second).

The main reason behind the improvement in the torque coefficient after the stall is due to the delay of stall condition. The suction slot increases the torque coefficient and delays the stall angle which further leads to an increase of first law efficiency. On the other hand, it increases the entropy generation rate which leads to decreasing the second law efficiency. The main reason also behind this increase in the entropy generation rate is due to the increases in velocity magnitude around the aerofoil lead to increase also in the entropy generation. Where, the entropy value depends on the velocity gradient. At the present study, the optimization parameters have been varied within a certain range with a fixed increment and all parameter values have been analyzed. An alternative approach that could save time and effort would be to use an automated optimization technique, [98]. Furthermore, Wells turbine impeller using the suction slot with optimum parameters needs to be investigated experimentally in the future. Finally, the operating conditions for the northern coast of Egypt are very suitable for the oscillating system with Wells turbine as a wave energy extractor. So, it is essential that to look at the wave energy in Egypt as the way to reduce fossil fuel usage.

6. Acknowledgements

The authors would like to acknowledge the support provided by the Department of Naval Architecture, Ocean and Marine Engineering at Strathclyde University, UK and the Department of Marine Engineering at Arab Academy for Science, Technology and Maritime Transport. The authors would like to thank Prof. Mohamed Abbas Kotb for his kind support and guidance.

References

[1] Mamun M. The Study on the Hysteretic Characteristics of the Wells Turbine in a Deep Stall Condition [PhD]. Japan: Saga University, 2006.
[2] Rosa AVd. Fundamentals of Renewable Energy Processes. Third Edition ed. United States of America: Elsevier Academic Press, 2012.
[3] Falcão AFdO. Wave energy utilization: A review of the technologies. Renewable and Sustainable Energy Reviews. 2010;14(3):899-918.
[4] Twidell J, Weir T. Renewable Energy Resources. Second edition ed. New York, USA: Taylor & Francis, 2006.
[5] Curran R, M. Folley Air turbine design for OWCs. In: Cruz iJ, editor. Ocean Wave Energy. Springer, Berlin. 2008. p. 189-219.
[6] Shehata AS, Xiao Q, Saqr KM, Naguib A, Alexander D. Passive flow control for aerodynamic performance enhancement of airfoil with its application in Wells turbine – Under oscillating flow condition. Ocean Engineering. 2017;136:31–53.
[7] T. J. T. Whittaker JGL, A. E. Long and M. A. Murray. The Queen's university of Belfast Axisymmetric and Multi-resonant Wave Energy Converters. Trans ASME J Energy Resources Tech. 1985;107: pp. 74-80.
[8] T. J. T. Whittaker FAM. Design Optimisation of Axisymmetric Tail Tube Buoys. IUTAM, Symposium on Hydrodynamics of Ocean Wave Energy Conversion. Lisbon,July.1985.
[9] Whittaker TJJ, McIlwain, S. T. and Raghunathan, S. . Islay Shore Line Wave Power Station. Proceedings European Wave Energy Symposium. 1993;Paper G6, Edinburgh.
[10] Raghunathan S. Theory and Performance of Wells Turbine. Queen's University of Belfast. 1980;Rept. WE/80/13R.
[11] Starzmann R. Aero-acoustic Analysis of Wells Turbines for Ocean Wave Energy Conversion [Doctoral]. Germany: Universitat Siegen, 2012.
[12] Shehata AS, Xiao Q, Saqr KM, Alexander D. Wells turbine for wave energy conversion: a review. International journal of energy research. 2017;41(1):6-38.
[13] IA B. Apparatus for Converting Sea Wave Energy into Electrical Energy. US Patent 3,922,739 1975;2 December 1975.
[14] Setoguchi T TM, Kinoue Y, Kaneko K, Santhakumar S, Inoue M. . Study on an impulse turbine for wave energy conversion. International Journal Offshore Polar Eng. 2000;10(2):145-52.
[15] T. Setoguchi SS, H. Maeda, M. Takao and K. Kaneko. A Review of Impulse Turbine for Wave Energy Conversion. Renewable Energy. 2001;23(2):261-92.
[16] T. Setoguchi MT, S. Santhakumar and K. Kaneko. Study of an Impulse Turbine for Wave Power Conversion: Effects of Reynolds Number and Hub-to-Tip Ratio on Performance. Journal of Offshore Mechanics and Arctic Engineering. 2004;126(2):137-40.

[17] Okuhara S, Takao M, Takami A, Setoguchi T. Wells Turbine for Wave Energy Conversion — Improvement of the Performance by Means of Impulse Turbine for Bi-Directional Flow. Open Journal of Fluid Dynamics. 2013;03(02):36-41.
[18] Raghunathan S. The Wells Air Turbine for Wave Energy Conversion. Progress Aerospace Sciences. 1995;31:335-86.
[19] Raghunathan S. A methodology for Wells turbine design for wave energy conversion. ARCHIVE: Proceedings of the Institution of Mechanical Engineers, Part A: Journal of Power and Energy 1990-1996 (vols 204-210). 1995;209(31):221-32.
[20] Dhanasekaran TS, Govardhan M. Computational Analysis of Performance and Flow Investigation on Wells Turbine for Wave Energy Conversion. Renewable Energy. 2005;30(14):2129-47.
[21] Brito-Melo A, Gato LMC, Sarmento AJNA. Analysis of Wells turbine design parameters by numerical simulation of the OWC performance. Ocean Engineering. 2002;29:1463–77.
[22] Masami Suzuki, Arakawa C. Design Method of Wave Power Generating System with Wells Turbine. Twelfth InternationalOffshoreandPolarEngineeringConference. Kitakyushu,Japan: The International Society of Offshore and Polar Engineers; 2002. p. 527-33.
[23] Camporeale SM, Filianoti P, Torresi M. Performance of a Wells turbine in a OWC device in comparison to laboratory tests. the Ninth European Wave and Tidal Energy Conference (EWTEC). Southampton, UK2011.
[24] Camporeale SM, Filianoti P. Behaviour of a small Wells turbine under randomly varying oscillating flow. the 8th European Wave and Tidal Energy Conference EWTEC. Uppsala, Sweden2009. p. 690-6.
[25] Taha Z, Sugiyono, Sawada T. A comparison of computational and experimental results of Wells turbine performance for wave energy conversion. Applied Ocean Research. 2010;32(1):83-90.
[26] Shehata AS, Saqr KM, Shehadeh M, Xiao Q, Day AH. Entropy Generation Due to Viscous Dissipation around a Wells Turbine Blade: A Preliminary Numerical Study. Energy Procedia. 2014;50:808-16.
[27] Shehata AS, Saqr KM, Xiao Q, Shehadeh MF, Day A. Performance Analysis of Wells Turbine Blades Using the Entropy Generation Minimization Method. Renewable Energy33-86:1123;2016 ..
[28] Christopher Koroneos, Thomas Spachos, Moussiopoulos N. Exergy analysis of renewable energy sources. Renewable Energy. 2003;28(2003):295–310.
[29] Shaaban S. Insight Analysis of Biplane Wells Turbine Performance. Energy Conversion and Management. 2012;59:50-7.
[30] Soltanmohamadi R, Lakzian E. Improved design of Wells turbine for wave energy conversion using entropy generation. Meccanica, Springer Netherlands. 2015;51(8):1713-22.
[31] Miguel AF, Aydin M. Ocean energy: exergy analysis and conversion. The Global Conferance on Global Warming. Lison, Portugal2011.
[32] Vosough A, Sadegh V. Different Kind of Renewable Energy and Exergy Concept. INTERNATIONAL JOURNAL OF MULTIDISCIPLINARY SCIENCES AND ENGINEERING. 2011;2(9).
[33] Pope K, Dincer I, Naterer GF. Energy and Exergy Efficiency Comparison of Horizontal and Vertical Axis Wind Turbines. Renewable Energy. 2010;35(9):2102-13.
[34] Baskut O, Ozgener O, Ozgener L. Effects of Meteorological Variables on Exergetic Efficiency of Wind Turbine Power Plants. Renewable and Sustainable Energy Reviews. 2010;14(9):3237-41.
[35] Redha AM, Dincer I, Gadalla M. Thermodynamic Performance Assessment of Wind Energy Systems: An Application. Energy. 2011;36(7):4002-10.
[36] Ozgener O, Ozgener L. Exergy and Reliability Analysis of Wind Turbine Systems: A Case Study. Renewable and Sustainable Energy Reviews. 2007;11(8):1811-26.
[37] Baskut O, Ozgener O, Ozgener L. Second Law Analysis of Wind Turbine Power Plants: Cesme, Izmir Example. Energy. 2011;36(5):2535-42.

[38] Mortazavi SM, Soltani MR, Motieyan H. A Pareto optimal multi-objective optimization for a horizontal axis wind turbine blade airfoil sections utilizing exergy analysis and neural networks. Journal of Wind Engineering and Industrial Aerodynamics. 2015;136:62-72.
[39] Şöhret Y, Açıkkalp E, Hepbasli A, Karakoc TH. Advanced exergy analysis of an aircraft gas turbine engine: Splitting exergy destructions into parts. Energy. 2015;90:1219-28.
[40] Ghazikhani M, Khazaee I, Abdekhodaie E. Exergy analysis of gas turbine with air bottoming cycle. Energy. 2014;72:599-607.
[41] Lugo-Leyte R, Salazar-Pereyra M, Méndez H, Aguilar-Adaya I, Ambriz-García J, Vargas J. Parametric Analysis of a Two-Shaft Aeroderivate Gas Turbine of 11.86 MW. Entropy. 2015;17(8):5829-47.
[42] Yousefi K, Saleh R, Zahedi P. Numerical study of blowing and suction slot geometry optimization on NACA 0012 airfoil. Journal of Mechanical Science and Technology. 2014;28(4):1297-310.
[43] Chapin VG, Benard E. Active Control of a Stalled Airfoil Through Steady or Unsteady Actuation Jets. Journal of Fluids Engineering. 2015;137(9):091103.
[44] Schatz M, G¨unther B, Thiele F. Computational Investigation of Separation Control for High-Lift Airfoil Flows. Berlin, Germany2007.
[45] Chawla JS, Suryanarayanan S, Puranik B, Sheridan J, Falzon BG. Efficiency improvement study for small wind turbines through flow control. Sustainable Energy Technologies and Assessments. 2014;7:195-208.
[46] Fernandez E, Kumar R, Alvi F. Separation Control on a Low-Pressure Turbine Blade using Microjets. Journal of Propulsion and Power. 2013;29(4):867-81.
[47] Volino RJ, Kartuzova O, Ibrahim MB. Separation Control on a Very High Lift Low Pressure Turbine Airfoil Using Pulsed Vortex Generator Jets. Journal of Turbomachinery. 2011;133(4):041021.
[48] Schlichting H. Boundary layer theory. McGraw-Hill, New York, USA. 1968: 347-62.
[49] Richards EJ, Burge CH. An airfoil designed to give laminar flow over the surface with boundary layer suction. Aeronautical Research Council, R&M 2263. 1943.
[50] Walker SW, Raymer WG. Wind tunnel test on the 30 percent symmetrical griffth aerofoil with ejection of air. Aeronautical Research Council, R&M 2475. 1946.
[51] Braslow AL. A history of suction type laminar flow control with emphasis on flight research, NASA History Division. Monograph in Aerospace History. 1999;13.
[52] L. Bahi JMR, Nagamatsu HT. Passive Shock Wave/Boundary Layer Control for Transonic Airfoil Drag Reduction. AIAA Journal. 1983;1983-0137.
[53] Savu G, Trifu O. Porous Airfoils in Transonic Flow. AIAA Journal. 1984;22:989-91.
[54] Huang L, Huang PG, LeBeau RP. Numerical study of blowing and suction control mechanism on NACA0012 airfoil. Journal of Aircraft. 2004;41(5): 1005-13.
[55] Greenblatt D, Wygnanski IJ. Control of flow separation by periodic excitation. Progress in Aerospace Sciences. 2000;36:487-545.
[56] Bushnell DM, McGinley CB. Turbulence Control in Wall Flows. Annual Review of Fluid Mechanics. 1989;21:1-20.
[57] Fiedler HE, Fernholz H-H. On Management and Control of Turbulent Shear Flows. Progress in Aerospace Sciences. 1990;27:305-87.
[58] Gad-el-Hak M, Bushnell DM. Separation Control: Review. Journal of Fluids Engineering. 1991;113:5-30.
[59] Moin P, Bewley T. Feedback Control of Turbulence. Applied Mechanics Reviews. 1994;47:S3-S13.
[60] Gad-el-Hak M. Interactive Control of Turbulent Boundary Layers: A Futuristic Overview. AIAA Journal. 1994;32:1753-65.
[61] Kim SH, Kim C. Separation control on NACA23012 using synthetic jet. Aerospace Science and Technology. 2009;13(4):172-82.

[62] Rumsey CL, Nishino T. Numerical study comparing RANS and LES approaches on a circulation control airfoil. International Journal of Heat and Fluid Flow. 2011;32(5):847-64.
[63] B. Yagiz, Kandil O, Pehlivanoglu YV. Drag minimization using active and passive flow control techniques. Aerospace Science and Technology. 2012;17(1):21-31.
[64] Shehata AS, Xiao Q, El-Shaib M, Sharara A, Alexander D. Comparative analysis of different wave turbine designs based on conditions relevant to northern coast of Egypt. Energy. 2017;120:450-67.
[65] Mørk G, Barstow S, Kabuth A, Pontes MT. ASSESSING THE GLOBAL WAVE ENERGY POTENTIAL. 29th International Conference on Ocean, Offshore Mechanics and Arctic Engineering. Shanghai, China: ASME; 2010.
[66] Barstow S, Mørk G, Lønseth L, Mathisen JP. WorldWaves wave energy resource assessments from the deep ocean to the coast. The 8th European Wave and Tidal Energy Conference. Uppsala, Sweden: Proceedings of the 8th European Wave and Tidal Energy Conference; 2009.
[67] Ayat B. Wave power atlas of Eastern Mediterranean and Aegean Seas. Energy. 2013;54:251-62.
[68] Zodiatis G, Galanis G, Nikolaidis A, Kalogeri C, Hayes D, Georgiou GC, et al. Wave energy potential in the Eastern Mediterranean Levantine Basin. An integrated 10-year study. Renewable Energy. 2014;69:311-23.
[69] SB. P. Turbulent flows. Cambridge University Press. 2000.
[70] DAHLSTROM S. LARGE EDDY SIMULATION OF THE FLOW AROUND A HIGH-LIFT AIRFOIL. Goteborg, Sweden: CHALMERS UNIVERSITY OF TECHNOLOGY, 2003.
[71] Moin P SK, Cabot W, Lee S. A dynamic subgrid-scale model for compressible turbulence and scalar transport. Physics Fluids A. 1991;3(11):2746–57.
[72] DK. L. A proposed modification of the Germano subgrid-scale closure method. Physics Fluids A. 1992;4(3):633–5.
[73] Hinze JO. Turbulence. New York: McGraw-Hill Publishing Co., 1975.
[74] Launder BE, Spalding DB. Lectures in Mathematical Models of Turbulence. London, England: Academic Press, 1972.
[75] Mamun M, Kinoue Y, Setoguchi T, Kim TH, Kaneko K, Inoue M. Hysteretic Flow Characteristics of Biplane Wells Turbine. Ocean Engineering. 2004;31(11-12):1423-35.
[76] Kinoue Y, Kim TH, Setoguchi T, Mohammad M, Kaneko K, Inoue M. Hysteretic Characteristics of Monoplane and Biplane Wells Turbine for Wave Power Conversion. Energy Conversion and Management. 2004;45(9-10):1617-29.
[77] Sheldahl RE, Klimas PC. Aerodynamic Characteristics of Seven Symmetrical Airfoil Sections Through 180-Degree Angle of Attack for Use in Aerodynamic Analysis of Vertical Axis Wind Turbines. Sandia National Laboratories energy report. the United States of America1981. p. 118.
[78] Bejan A. Entropy Generation Minimization- The New Thermodynamics of Finite-Size Devices and Finite-Time Processes. Applied Physics Reviews. 1996;79(3):1191-218.
[79] A. Stodola. Steam and Gas Turbines (McGraw-Hill, New York). 1910.
[80] Iandoli CL. 3-D Numerical Calculation of the Local Entropy Generation Rates in a Radial Compressor Stage. International journal of thermodynamics. 2005;8:83-94.
[81] Smagorinsky J. General Circulation Experiments with the Primitive Equations. I. The Basic Experiment. Month Wea Rev. 1963;91:pp.99-164.
[82] Tae-Hun Kim, Yeon- Won Lee, Ill-Kyoo Park, Toshiaki Setoguchi, Kang C-S. Numerical Analysis for Unsteady Flow Characteristics of the Wells Turbine. International Offshore and Polar Engineering Conference. Kitakyushu, Japan: The International Society of Offshore and Polar Engineers; 2002. p. 694-9.
[83] Nomura T, Suzuki Y, Uemura M, Kobayashi N. Aerodynamic Forces on a Square Cylinder in Oscillating Flow with Mean Velocity. Journal of Wind Engineering and Industrial Aerodynamics. 2003;91:199–208.
[84] Setoguchi T, Kinoue Y, Kim TH, Kaneko K, Inoue M. Hysteretic Characteristics of Wells Turbine for Wave Power Conversion. Renewable Energy. 2003;28(13):2113-27.

[85] Kinoue Y, Setoguchi T, Kim TH, Kaneko K, Inoue M. Mechanism of Hysteretic Characteristics of Wells Turbine for Wave Power Conversion. Journal of Fluids Engineering. 2003;125(2):302.
[86] DE Moura CAK, Carlos S. The Courant–Friedrichs–Lewy (CFL) Condition: 80 Years After Its Discovery. 1 ed. Boston: Birkhäuser Basel, 2013.
[87] Torresi M, Camporeale SM, Pascazio G. Detailed CFD Analysis of the Steady Flow in a Wells Turbine Under Incipient and Deep Stall Conditions. Journal of Fluids Engineering. 2009;131(7):071103.
[88] Kawai S, Asada K. Wall-modeled large-eddy simulation of high Reynolds number flow around an airfoil near stall condition. Computers & Fluids. 2013;85:105-13.
[89] Richez F, Mary I, Gleize V, Basdevant C. Zonal RANS/LES coupling simulation of a transitional and separated flow around an airfoil near stall. Theoretical and Computational Fluid Dynamics. 2007;22(3-4):305-15.
[90] Alferez N, Mary I, Lamballais E. Study of Stall Development Around an Airfoil by Means of High Fidelity Large Eddy Simulation. Flow, Turbulence and Combustion. 2013;91(3):623-41.
[91] Kim Y, Castro IP, Xie ZT. Large-Eddy Simulations for Wind Turbine Blade: Dynamic Stall and Rotational Augmentation. 2015;20:369-75.
[92] AlMutairi J, AlQadi I, ElJack E. Large Eddy Simulation of a NACA-0012 Airfoil Near Stall. 2015;20:389-95.
[93] Armenio V, Geurts B, Fröhlich J. Large Eddy Simulation of Flow Around an Airfoil Near Stall. 2010;13:541-5.
[94] Hitiwadi M, Dulini V, Mudunkotuwa Y, Chisachi K. Large Eddy Simulations of 2D and Open-tip Airfoils Using Voxel Meshes. Procedia Engineering. 2013;61:32-9.
[95] Bromby DYaW. Large-Eddy Simulation of Unsteady Separation Over a Pitching Airfoil at High Reynolds Number. Seventh International Conference on Computational Fluid Dynamics (ICCFD7). Big Island, Hawaii2012.
[96] Torresi M, Camporeale S, Pascazio G. Performance of a Small Prototype of a High Solidity Wells Turbine. Seventh European Conference on Turbomachinery Fluid Dynamics and Thermodynamics. Athens, Greece 2007.
[97] Torresi M, Camporeale S, Pascazio G. Experimental and Numerical Investigation on the Performance of a Wells Turbine Prototype. Seventh European Wave and Tidal Energy Conference. Porto, Portugal 2007.
[98] Selim MM, Koomullil RP, Shehata AS. Incremental approach for radial basis functions mesh deformation with greedy algorithm. Journal of Computational Physics. 2017;340:556-74.

Table 1 A summary of the performance data for the different turbines

Airfoil	NACA0015		HSIM 15-262123-1576	
Max. Efficiency	Without guide vanes	With guide vanes	Without guide vanes	With guide vanes
	58%	71%	55%	67%

Table 2 Maximum efficiency with minimum torque and starting torque coefficients

Turbine profile	Maximum efficiency	Minimum torque coefficient	Starting torque coefficient
R7N08N65 G15N11S40	44.8%	0.41	0.49
R7N08F65 G15N21S31	47.4%	0.08	0.33

Table 3 The error percentage between measured F_D from reference (Nomura, Suzuki et al. 2003) and calculated F_D from CFD under unsteady flow with sinusoidal inlet velocity

Frequency 2 Hz													
F_D **(gf)**	**Time (Second)**												
	14.02	14.1	14.12	14.2	14.3	14.34	14.4	14.5	14.6	14.7	14.8	14.9	15
Experimental	3.4	7.7	9.9	14.4	12.9	3.4	4.11	2.3	7.5	14.7	10.7	3.9	2.7
CFD	3.8	7.8	9.8	14.5	12.5	3.5	3.4	2.7	7.8	14.9	10.9	3.8	2.4
Error %	11	1	-1	1	-4	1	-17	17	4	1	2	-2	-11
Frequency 1 Hz													
Experimental	4.5	6.9	12.6	14.1	14.3	13	10.2	7.8	4.7	2.8	2.3	2.5	3
CFD	4.6	7.2	12.6	13.1	14.3	13.2	10.3	8.6	4.5	2.7	2.2	2.6	3.3
Error %	2	4	0	-7	0	1	1	10	-4	1	-4	4	10

Table 4 Two suction slots with P_{ss} and ΔP_{ss} equal to 0.05

Reference suction slot	Location of second suction slot															Max. value %
	20%	25%	30%	35%	40%	45%	50%	55%	60%	65%	70%	75%	80%	85%	90%	
R 20%	-	0.121	0.083	0.12	0.102	0.13	0.126	0.123	0.117	0.11	0.101	0.102	0.094	0.1	0.087	56
R 25%	0.121	-	0.126	0.124	0.121	0.12	0.123	0.146	0.122	0.114	0.117	0.125	0.108	0.11	0.115	76
R 30%	0.083	0.126	-	0.125	0.123	0.14	0.118	0.119	0.127	0.118	0.113	0.121	0.117	0.11	0.1	65
R 35%	0.12	0.124	0.125	-	0.133	0.15	0.125	0.122	0.134	0.125	0.138	0.119	0.116	0.12	0.107	74
R 40%	0.102	0.121	0.123	0.133	-	0.15	0.144	0.148	0.136	0.133	0.127	0.137	0.134	0.14	0.142	81
R 45%	0.129	0.123	0.137	0.145	0.151	-	0.131	0.131	0.132	0.137	0.123	0.137	0.128	0.12	0.106	81
R 50%	0.126	0.123	0.118	0.126	0.144	0.13	-	0.125	0.138	0.142	0.137	0.127	0.138	0.13	0.134	74
R 55%	0.123	0.146	0.119	0.122	0.148	0.13	0.125	-	0.114	0.122	0.104	0.121	0.131	0.13	0.126	78
R 60%	0.117	0.122	0.127	0.134	0.136	0.13	0.138	0.114	-	0.108	0.13	0.136	0.128	0.11	0.115	66
R 65%	0.11	0.114	0.118	0.125	0.133	0.14	0.142	0.122	0.108	-	0.131	0.111	0.131	0.12	0.123	71
R 70%	0.101	0.117	0.113	0.138	0.127	0.12	0.137	0.104	0.13	0.131	-	0.116	0.117	0.11	0.113	66
R 75%	0.102	0.125	0.121	0.119	0.137	0.14	0.127	0.121	0.136	0.111	0.116	-	0.118	0.12	0.086	65
R 80%	0.094	0.108	0.117	0.116	0.134	0.13	0.138	0.131	0.128	0.131	0.117	0.118	-	0.12	0.1	66
R 85%	0.099	0.111	0.113	0.117	0.135	0.12	0.13	0.129	0.11	0.117	0.113	0.117	0.115	-	0.102	62
R 90%	0.087	0.115	0.1	0.107	0.142	0.11	0.134	0.126	0.115	0.123	0.113	0.086	0.1	0.10	-	71

Maximum value

Table 5 The value of improvement in torque coefficient for the optimum locations for two suction slots at different angles with non-oscillating velocity

Torque Coefficient	**Angle of attack (°)**							
	8.7	10.1	10.6	11.3	11.7	12.3	13.6	14.4
Without Suction Slot	0.0509	0.0669	0.0726	0.0793	0.0856	0.0910	0.0830	0.0676
Two Suction Slots at $L_{ss} = 40\%$ and $L_{ss} = 45\%$	0.0654	0.0904	0.0973	0.1122	0.1210	0.1300	0.1505	0.1420
Improvement %	28	35	34	42	41	43	81	110
Two Suction Slots at $L_{ss} = 40\%$ and $L_{ss} = 44\%$	0.0659	0.0848	0.0980	0.1087	0.1175	0.1238	0.1526	0.1428
Improvement %	29	27	35	37	37	36	84	111
Two Suction Slots at $L_{ss} = 45\%$ and $L_{ss} = 49\%$	0.0627	0.0923	0.1011	0.1095	0.1194	0.1297	0.1526	0.1444
Improvement %	23	38	39	38	39	43	84	114

Table 6 Three suction slots with P_{ss} and ΔP_{ss} equal to 0.05

Reference suction slot	Location of third suction slot												Max. value
	20%	25%	30%	35%	40%	45%	50%	55%	60%	65%	70%	75%	80%	85%	90%	
R 25% and R 55%	0.084	—	0.155	0.149	0.132	0.149	0.100	—	0.136	0.130	0.145	0.130	0.113	0.147	0.144	86%
R 35% and R 45%	0.130	0.131	0.104	—	0.143	—	0.137	0.142	0.140	0.133	0.127	0.142	0.130	0.136	0.138	72%
R 40% and R 45%	0.109	0.144	0.133	0.143	—	—	0.151	0.152	0.155	0.141	0.147	0.151	0.137	0.152	0.126	86%
R 40% and R 50%	0.121	0.104	0.139	0.129	—	0.151	—	0.137	0.146	0.151	0.146	0.142	0.140	0.137	0.144	82%
R 40% and R 55%	0.119	0.132	0.129	0.137	—	0.152	0.137	—	0.147	0.130	0.147	0.159	0.157	0.130	0.161	94%
R 40% and R 90%	0.083	0.135	0.135	0.142	—	0.126	0.144	0.161	0.140	0.137	0.138	0.129	0.140	0.129	—	94%
R 50% and R 65%	0.130	0.146	0.130	0.126	0.151	0.139	—	0.129	0.133	—	0.127	0.133	0.119	0.123	0.130	82%

Maximum value

Table 7 Three suction slots with $\boldsymbol{P_{ss}}$and $\Delta\boldsymbol{P_{ss}}$ equal to 0.01

Reference suction slot	Location of third suction slot											Max. value
	95%	94%	93%	92%	91%	90%	89%	88%	87%	86%	85%	
R 40% and R 55%	0.1577	0.1387	0.1369	0.1510	0.1536	0.1610	0.1543	0.1556	0.1542	0.138	0.130	94%
Reference suction slot	60%	59%	58%	57%	56%	55%	54%	53%	52%	51%	50%	Max. value
R 40% and R 90%	0.1397	0.1492	0.1437	0.1421	0.1414	0.1610	0.1425	0.1476	0.1423	0.124	0.144	94%
Reference suction slot	45%	44%	43%	42%	41%	40%	39%	38%	37%	36%	35%	Max. value
R 55% and R 90%	0.1318	0.1401	0.1433	0.1246	0.1386	0.1610	0.1553	0.1256	0.1306	0.125	0.125	94%

Maximum value

Table 8 Four suction slots with P_{ss} and ΔP_{ss} equal to 0.05

Reference suction slot	Location of fourth suction slot													Max. value
	20%	25%	30%	35%	40%	45%	50%	55%	60%	65%	70%	75%	80%	85%	90%	
R 25%, 30% and R 55%	0.143	—	—	0.151	0.13	0.142	0.124	—	0.155	0.122	0.144	0.155	0.123	0.148	0.156	88%
R 40%, 45% and R 50%	0.131	0.122	0.144	0.149	—	—	—	0.13	0.144	0.158	0.153	0.150	0.146	0.156	0.154	90%
R 40%, 45% and R 55%	0.141	0.137	0.132	0.137	—	—	0.143	—	0.160	0.135	0.157	0.151	0.156	0.155	0.125	92%
R 40%, 45% and R 60%	0.132	0.131	0.136	0.142	—	—	0.144	0.10	—	0.148	0.148	0.145	0.150	0.151	0.137	92%
R 40%, 45% and R 75%	0.121	0.148	0.133	0.144	—	—	0.150	0.11	0.145	0.147	0.135	—	0.149	0.145	0.147	82%
R 40%, 45% and R 85%	0.128	0.143	0.136	0.136	—	—	0.156	0.65	0.151	0.142	0.138	0.745	0.136	—	0.139	88%
R 40%, 50% and R 65%	0.147	0.134	0.125	0.140	—	0.158	—	0.13	0.140	—	0.101	0.148	0.142	0.128	0.147	90%
R 40%, 55% and R 75%	0.143	0.099	0.136	0.141	—	0.151	0.157	—	0.150	0.150	0.148	—	0.147	0.139	0.156	89%
R 40%, 55% and R 80%	0.137	0.134	0.131	0.133	—	0.125	0.122	—	0.139	0.151	0.138	0.147	—	0.141	0.136	82%
R 40%, 55% and R 90%	0.141	0.134	0.135	0.149	—	0.134	0.148	—	0.143	0.137	0.155	0.156	0.136	0.157	—	89%

Maximum value

Table 9 Four suction slots with $P_{ss}$and ΔP_{ss} equal to 0.01

Reference suction slot	Location of fourth suction slot										Max. value
	65%	**64%**	**63%**	**62%**	**61%**	**60%**	**59%**	**58%**	**57%**	**56%**	
R 40%, 45% and R 55%	0.1348	0.1396	0.1507	0.1477	0.1400	0.1596	0.1501	0.1316	0.1359	0.1229	92%
Reference suction slot	**59%**	**58%**	**57%**	**56%**	**55%**	**54%**	**53%**	**52%**	**51%**	**50%**	**Max. value**
R 40%, 45% and R 60%	0.1409	0.1368	0.1306	0.1376	0.1596	0.1410	0.1344	0.1411	0.1427	0.1441	92%
Reference suction slot	**50%**	**49%**	**48%**	**47%**	**46%**	**45%**	**44%**	**43%**	**42%**	**41%**	**Max. value**
R 40%, 55% and R 60%	0.1239	0.1326	0.1338	0.1366	0.1291	0.1596	0.1364	0.1253	0.1126	0.1349	92%
Reference suction slot	**44%**	**43%**	**42%**	**41%**	**40%**	**39%**	**38%**	**37%**	**36%**	**35%**	**Max. value**
R 45%, 55% and R 60%	0.1302	0.1073	0.1397	0.1421	0.1596	0.1438	0.1318	0.1387	0.1307	0.1369	92%

Maximum value

Table 10 The global entropy generation rate at different angles of attack with wave time period equal to 4 sec

S_G (W/K)	Angle of attack (°)				
	11.3	11.7	12.3	13.6	14.4
$L_{ss} = 40\%$ and $L_{ss} = 45\%$	0.066	0.066	0.067	0.074	0.063
Average value	Before the stall (6.6%)			After the stall (6.8%)	
$L_{ss} = 40\%$, $L_{ss} = 55\%$ and $L_{ss} = 90\%$	0.066	0.067	0.071	0.073	0.079
Average value	Before the stall (6.8%)			After the stall (7.6%)	

Table 11 The global entropy generation rate at different angles of attack with wave time period equal to 6 sec

S_G (W/K)	Angle of attack (°)				
	11.3	11.7	12.3	13.6	14.4
$L_{ss} = 40\%$ and $L_{ss} = 45\%$	0.065	0.067	0.067	0.068	0.062
Average value	Before the stall (6.6%)			After the stall (6.5%)	
$L_{ss} = 40\%$, $L_{ss} = 55\%$ and $L_{ss} = 90\%$	0.067	0.071	0.068	0.071	0.080
Average value	Before the stall (6.9%)			After the stall (7.6%)	

Table 12 The global entropy generation rate at different angles of attack with wave time period equal to 8 sec

S_G (W/K)	Angle of attack (°)				
	11.3	11.7	12.3	13.6	14.4
$L_{ss} = 40\%$ and $L_{ss} = 45\%$	0.064	0.063	0.064	0.070	0.064
Average value	Before the stall (6.4%)			After the stall (6.7%)	
$L_{ss} = 40\%$, $L_{ss} = 55\%$ and $L_{ss} = 90\%$	0.066	0.065	0.065	0.073	0.075
Average value	Before the stall (6.5%)			After the stall (7.4%)	

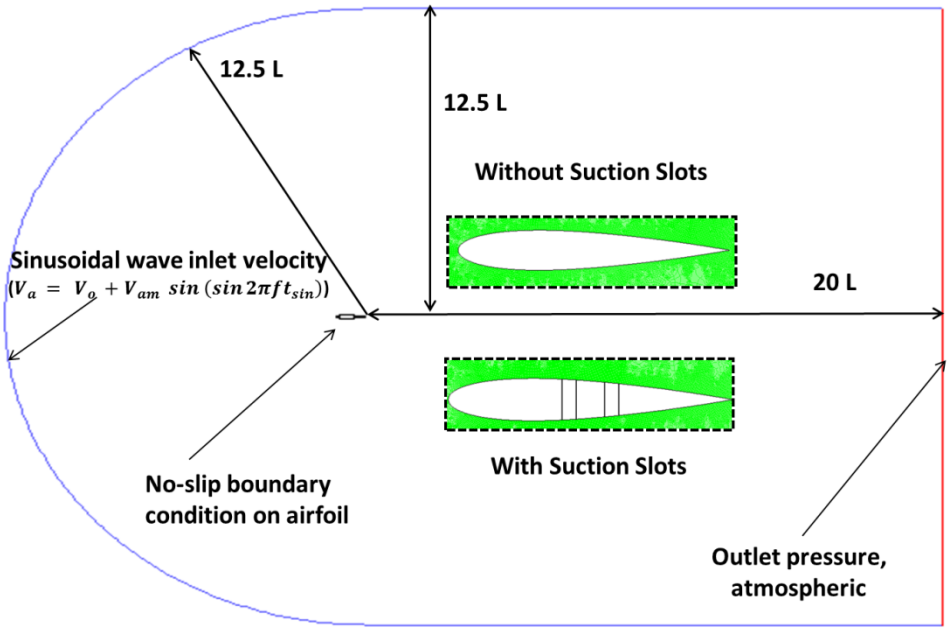

Figure 1 Dimensions of whole computational domain and location of airfoil.

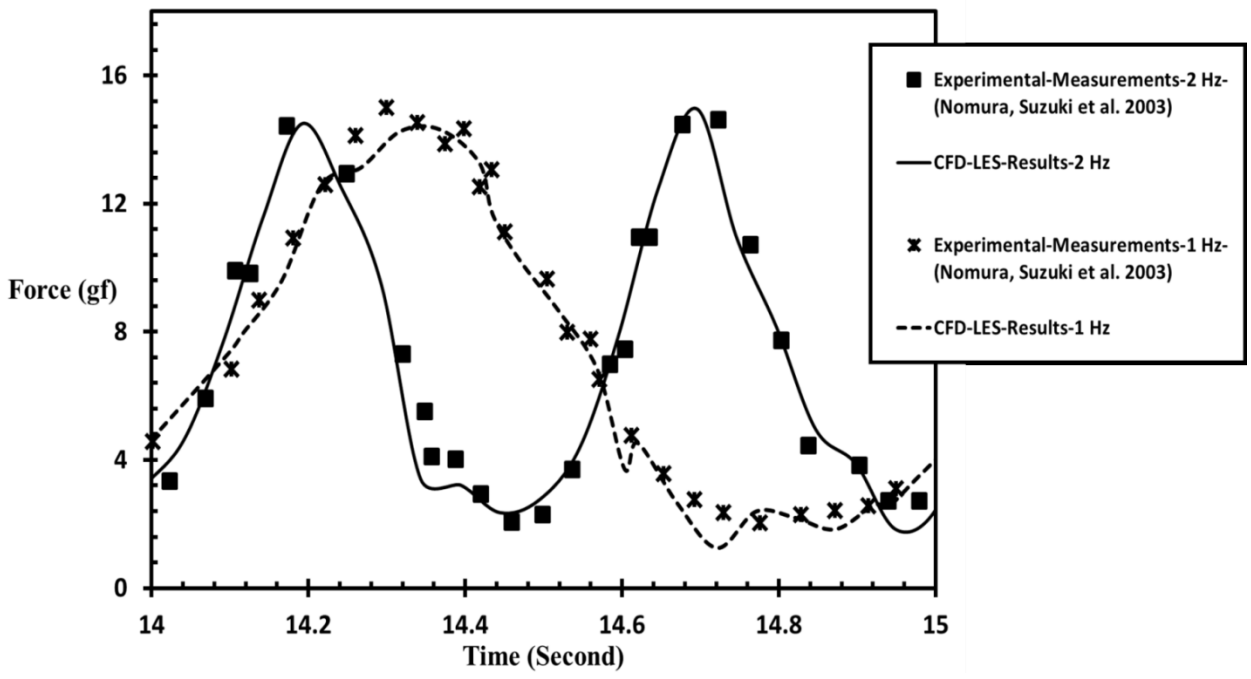

Figure 2 Measured unsteady in-line force F_D from reference (Nomura, Suzuki et al. 2003), (angle of attack= 0 º) and F_D calculated from the present CFD with frequencies 2 Hz and 1Hz.

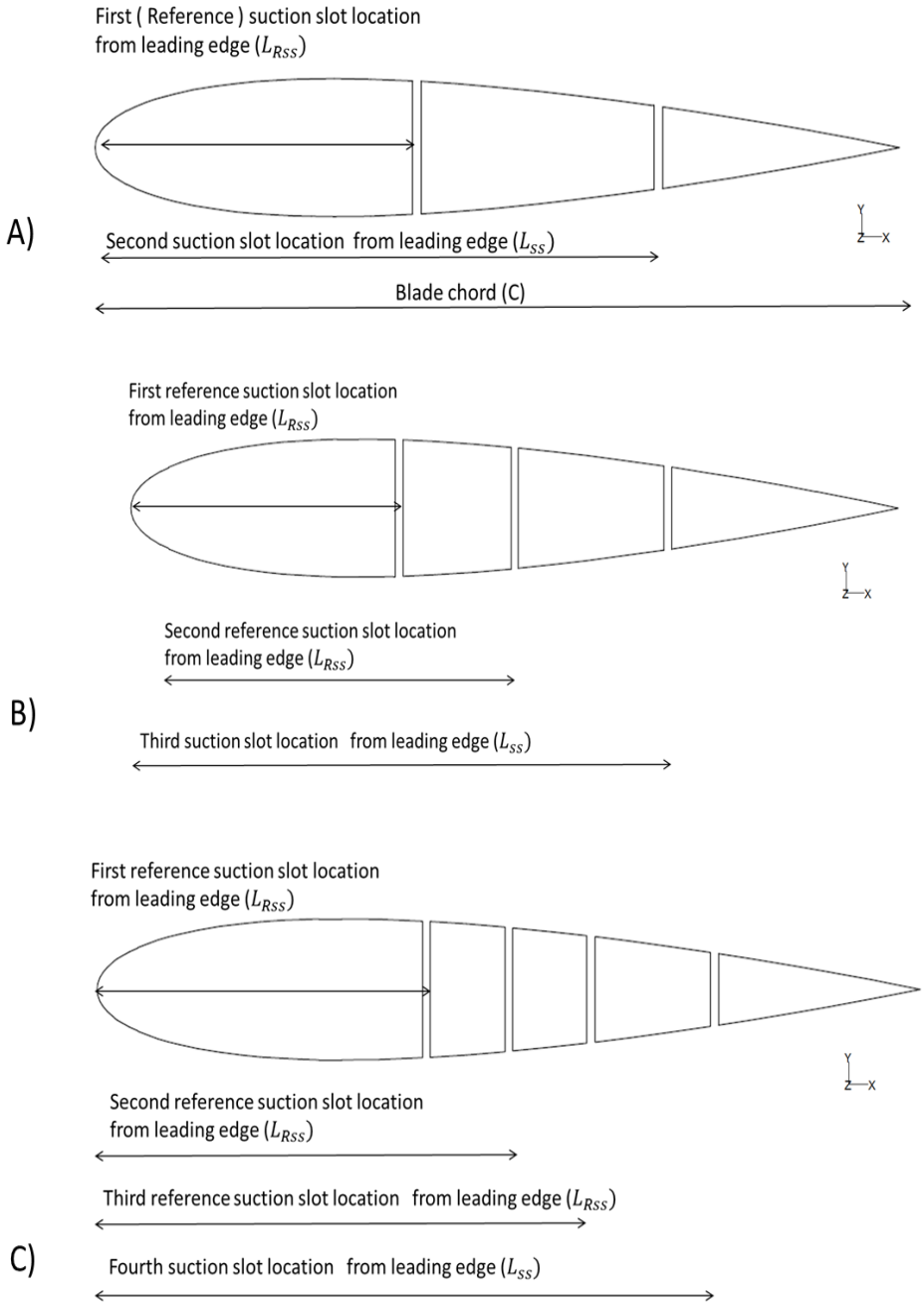

Figure 3 Aerofoil diagram with two, three and four suction slots A) Two suction slots B) Three suction slots C) four suction slots

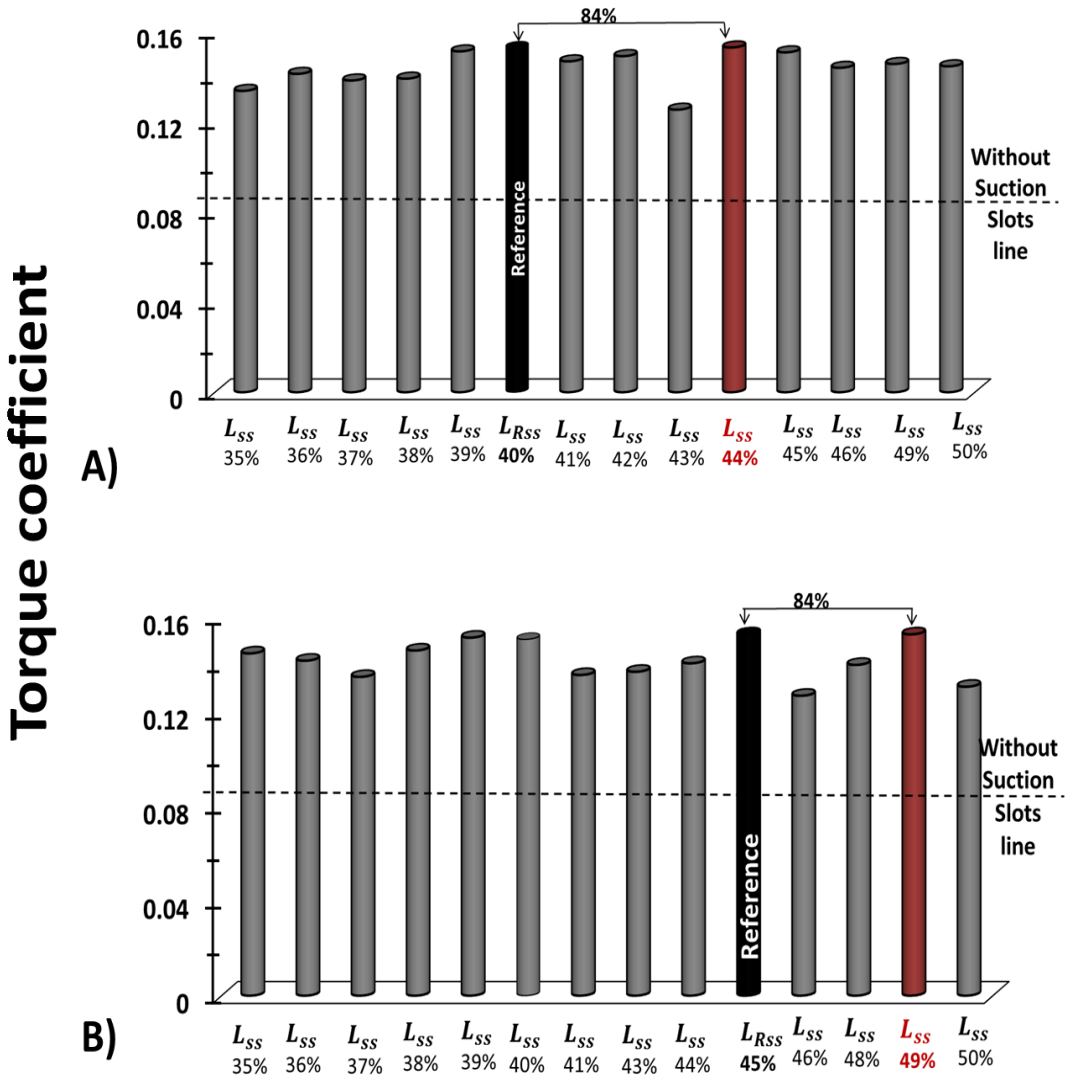

Figure 4 The effect of tow suction slots on the torque coefficient at the stall angle (13.6 °) with $\boldsymbol{P_{ss}}$and $\Delta\boldsymbol{P_{ss}}$ equal to 0.01 A) $\boldsymbol{L_{Rss}}$= 40% and 44%. B) $\boldsymbol{L_{Rss}}$= 45% and 49%

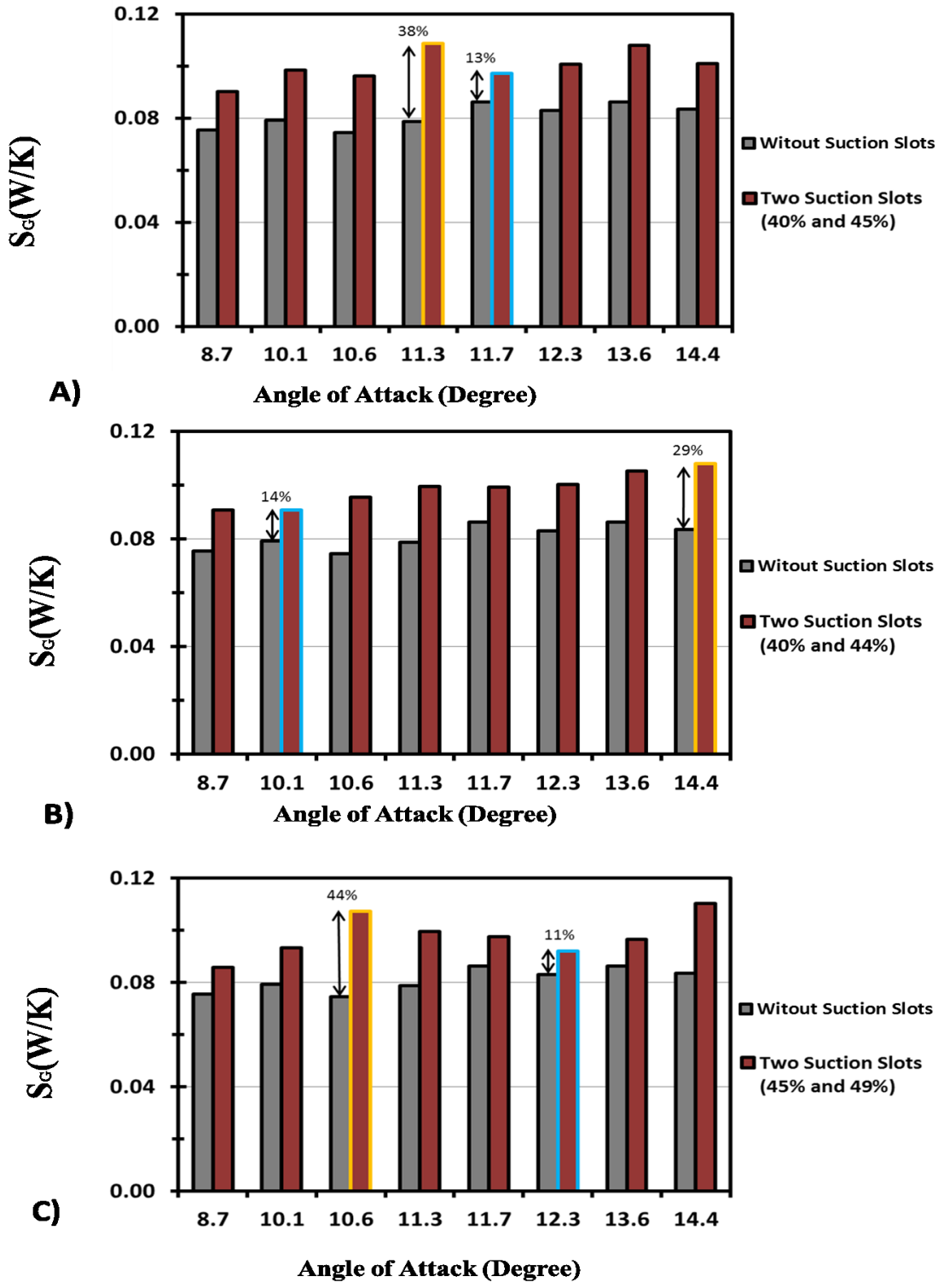

Figure 5 S_G for the optimum locations for two suction slots with non-oscillating velocity A) (L_{ss}40% and 45%) B) (L_{ss}40% and 44%). C) (L_{ss}45% and 49%)

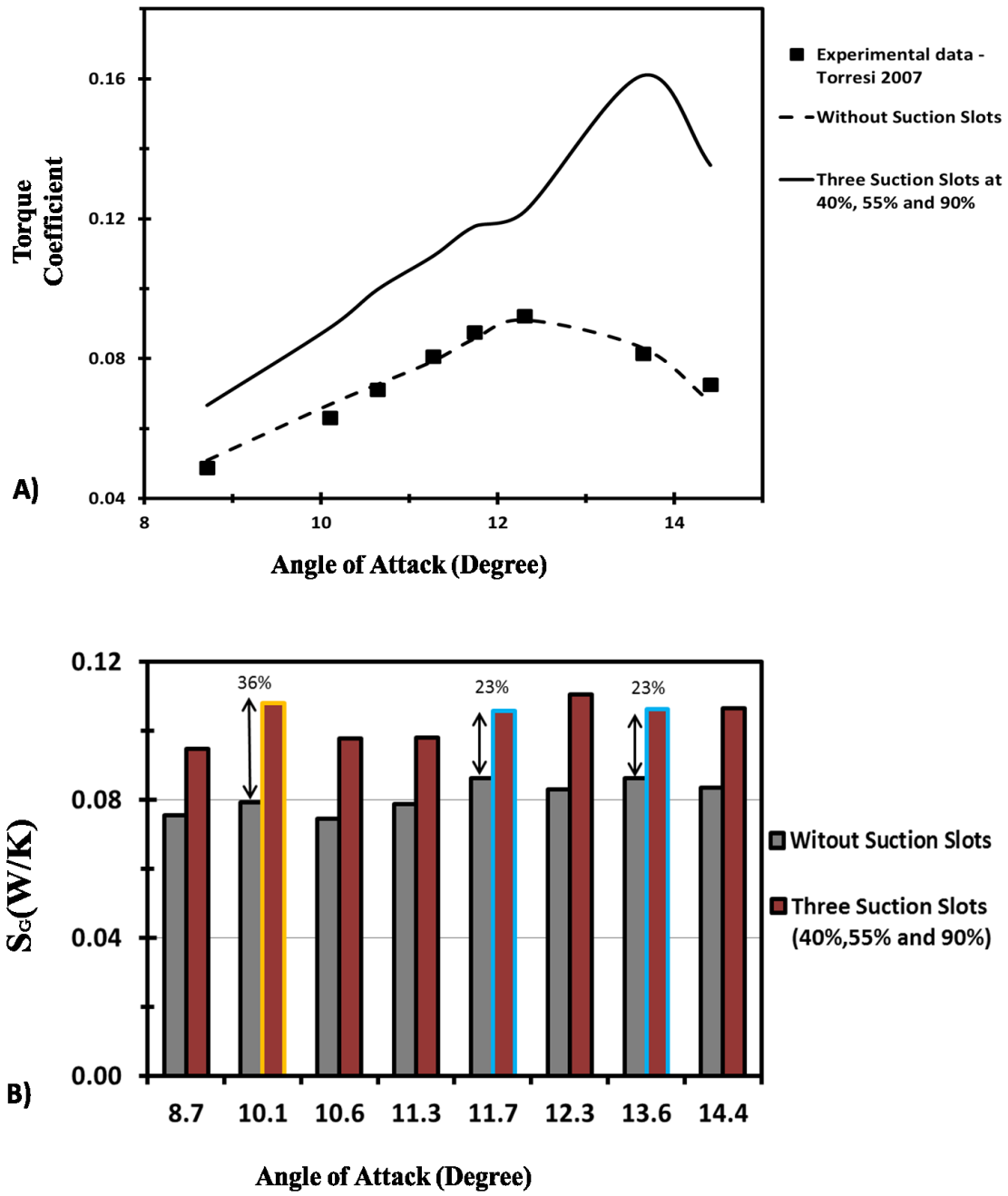

Figure 6 The optimum location for three suction slots at different angles with non-oscillating velocity. A) Torque coefficient. B) S_G

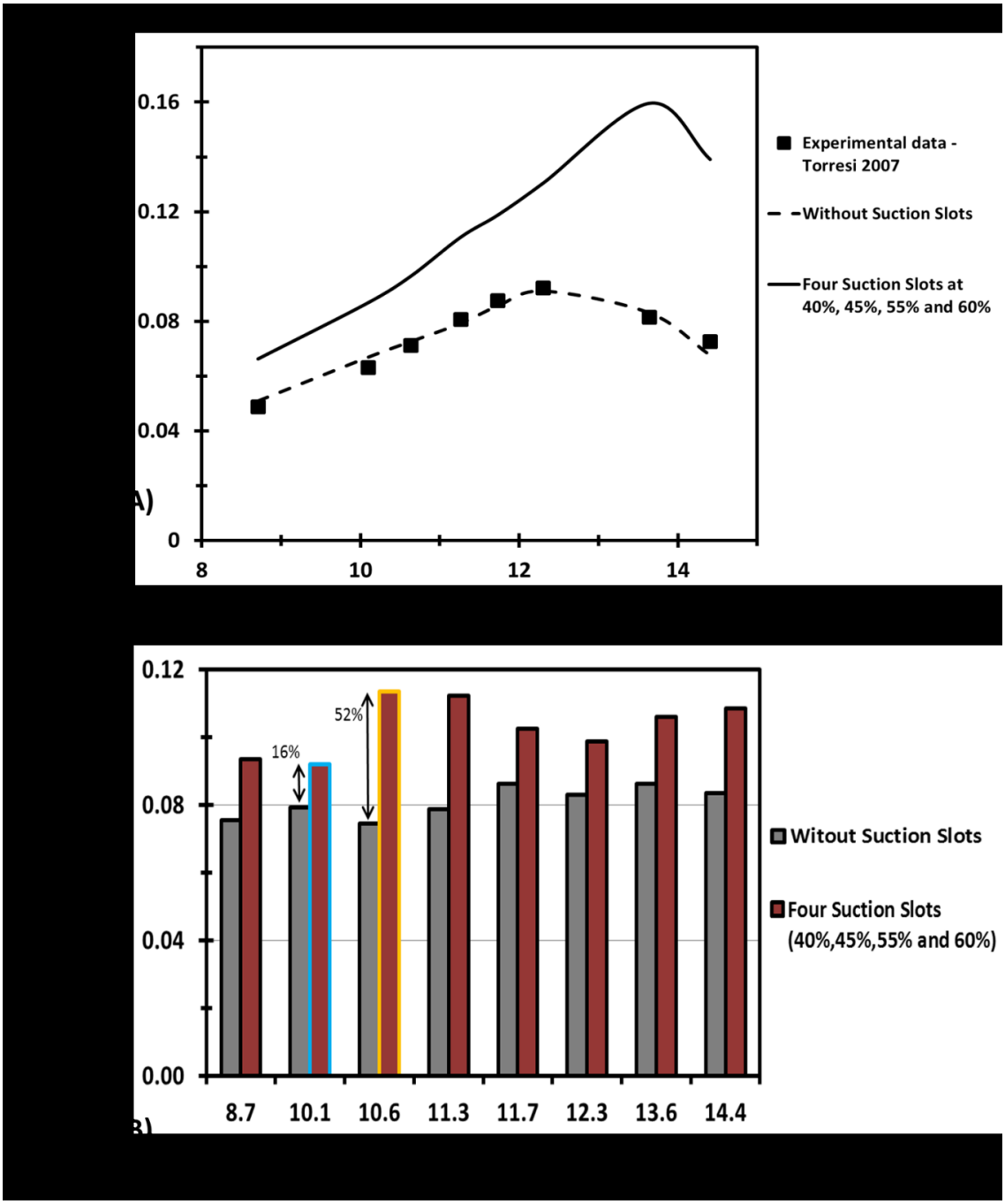

Figure 7 The optimum location for four suction slots at different angles with non-oscillating velocity A) Torque coefficient B) S_G

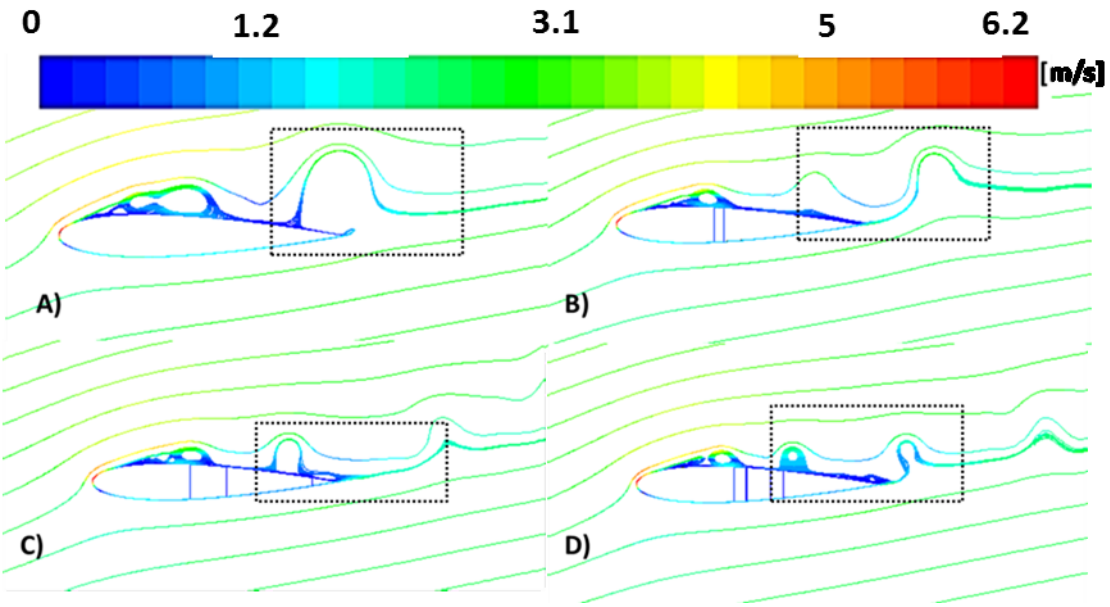

Figure 8 Path-line coloured by mean velocity magnitude at 13.6 º, A) NACA0015 without slots B) L_{ss}40% and 44% C) L_{ss}40%, 55% and 90% D) L_{ss}40%,45%, 55%, and 60%

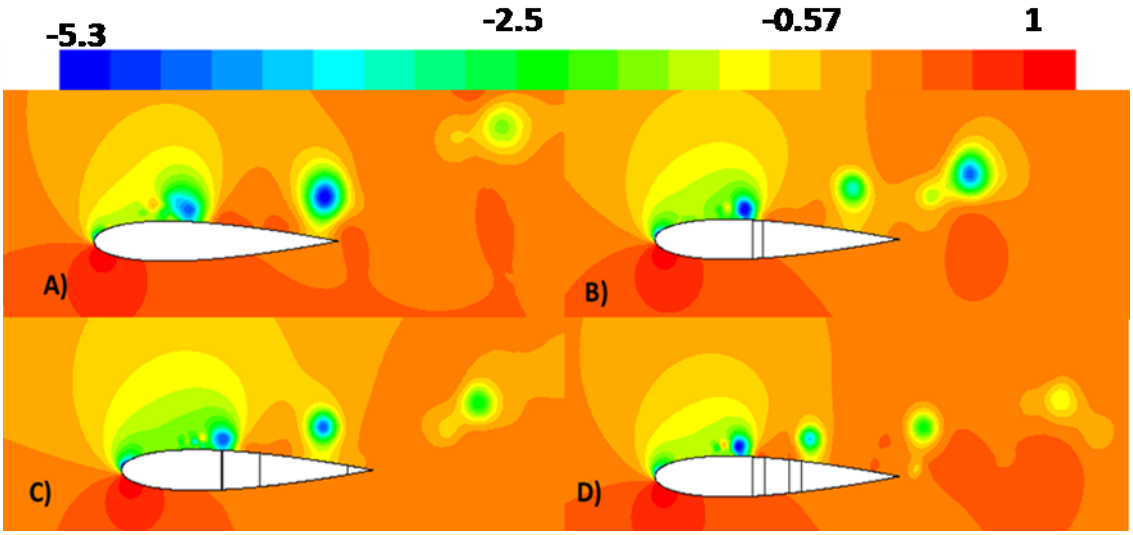

Figure 9 Contours of pressure coefficient around the aerofoil at 13.6 º, A) NACA0015 without slots B) L_{ss}40% and 44% C) L_{ss}40%, 55% and 90% D) L_{ss}40%,45%, 55%, and 60%

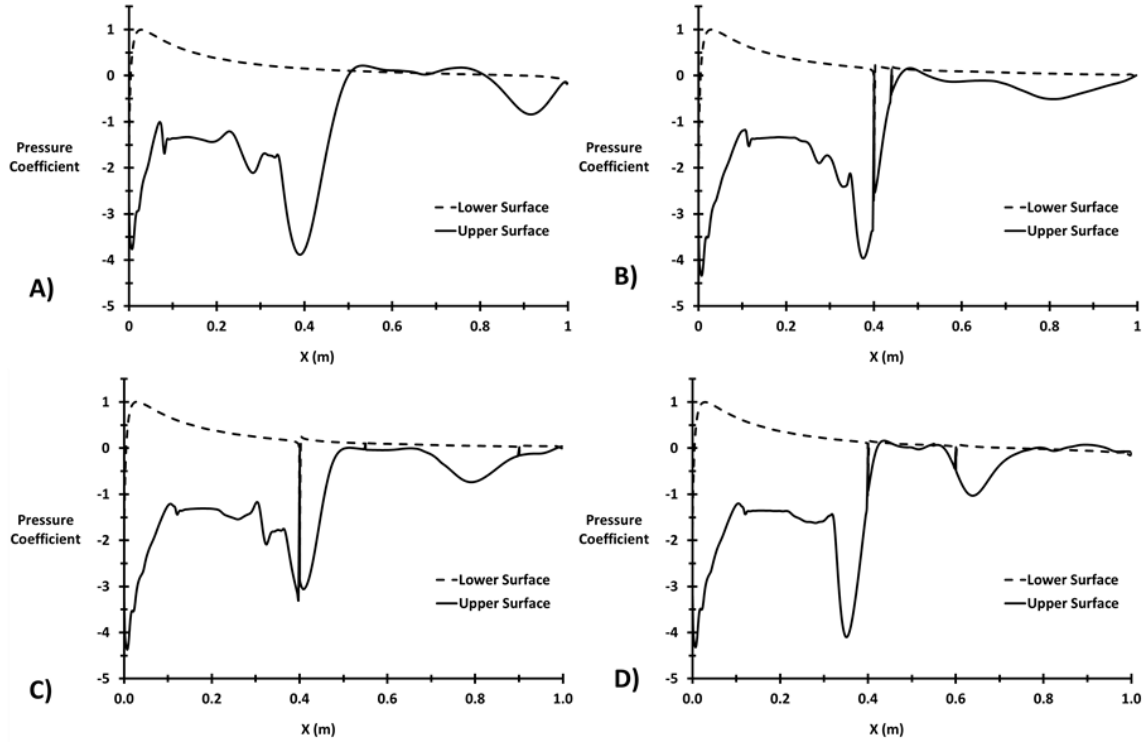

Figure 10 Pressure distribution on the upper and lower surface at 13.6 º, A) NACA0015 without slots B) L_{ss}40% and 44% C) L_{ss}40%, 55% and 90% D) L_{ss}40%,45%, 55%, and 60%

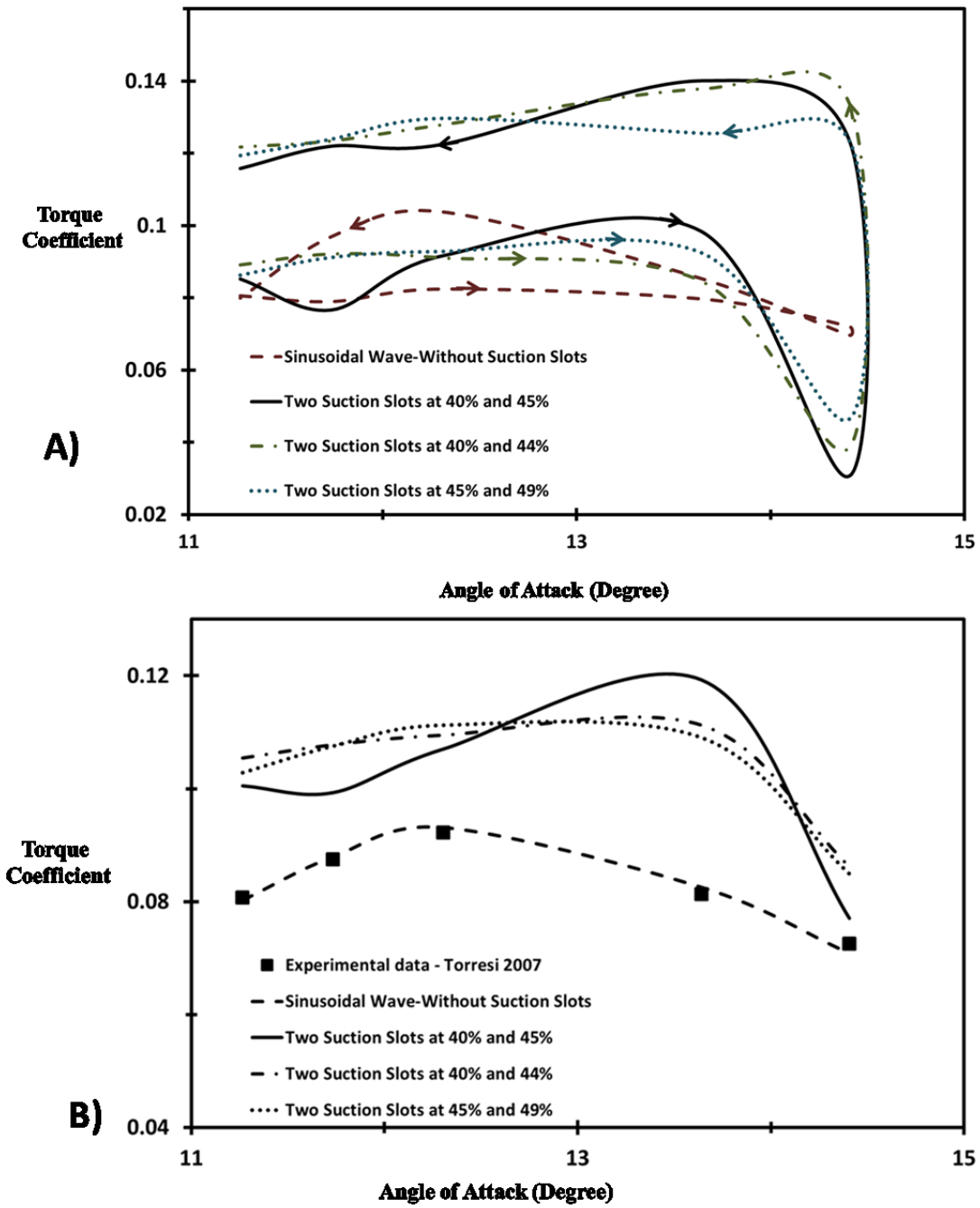

Figure 11 Comparison between the optimum locations for two suction slots at different angles with sinusoidal inlet velocity A) The hysteretic behaviour B) The average torque coefficient

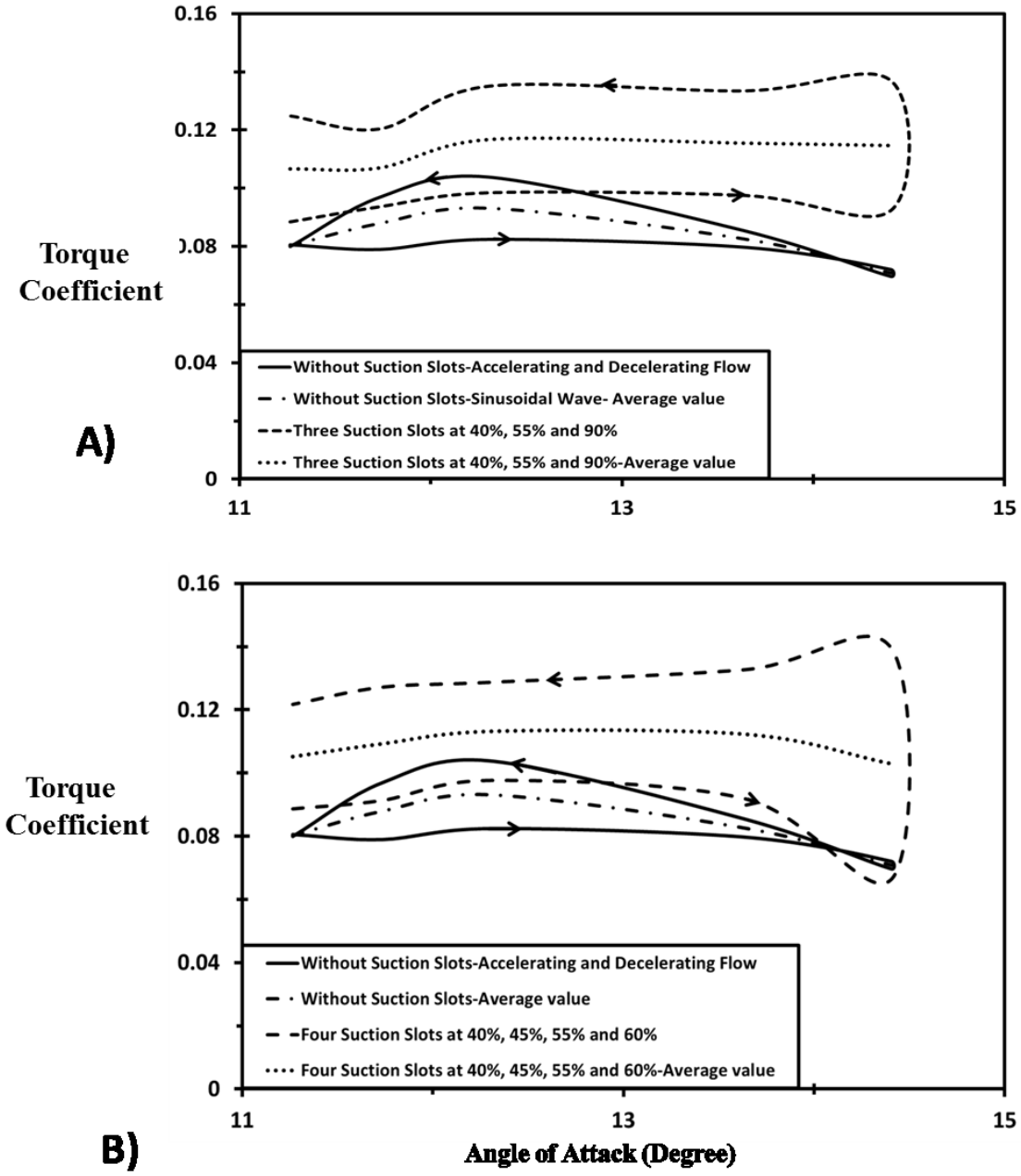

Figure 12 The hysteretic behaviour and the average torque coefficient for the optimum locations of the suction slots with sinusoidal velocity, A) Three suction slots B) Four suction slots

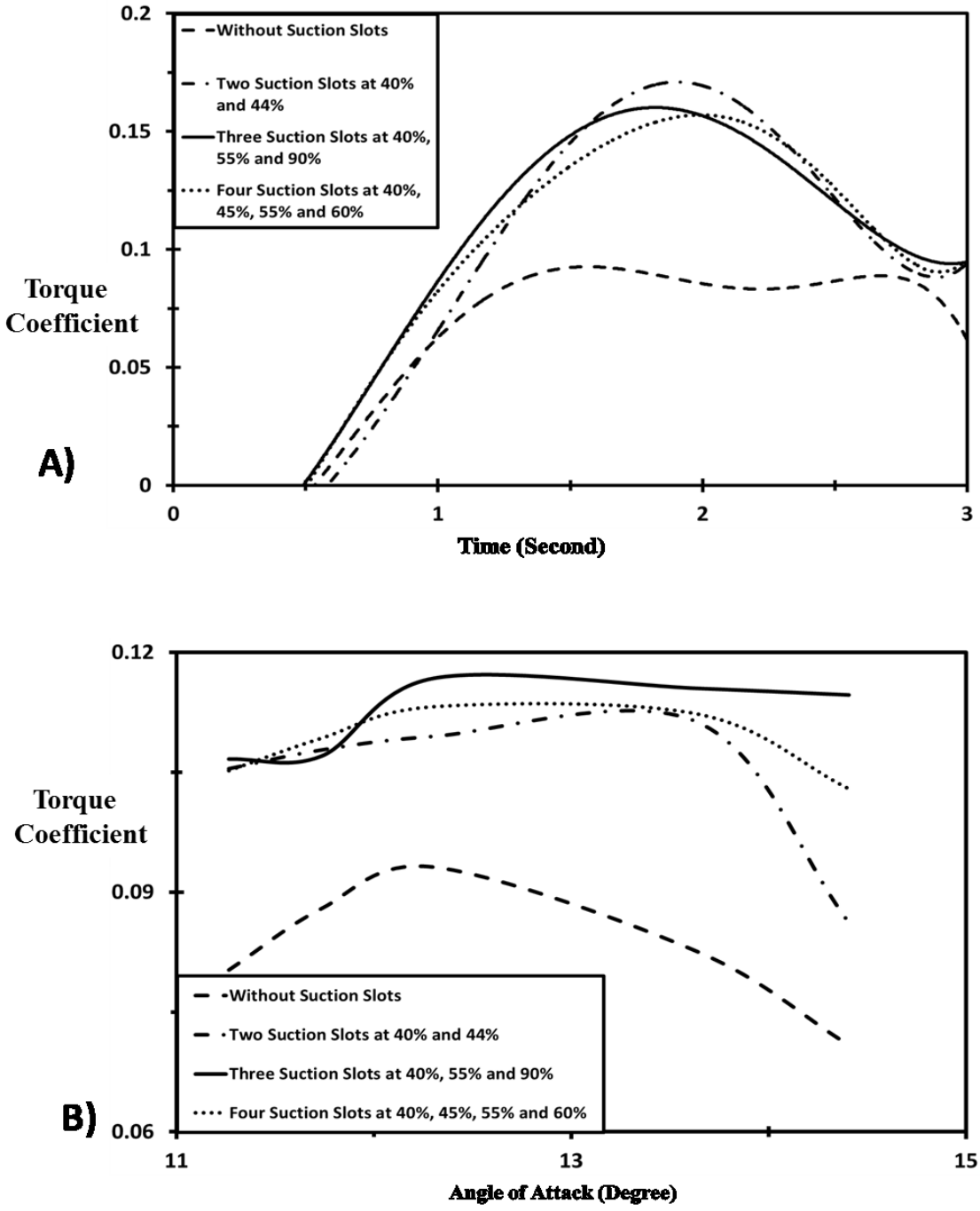

Figure 13 The comparison between the two suction slots, three suction slots and four suction slots A) The instantaneous torque coefficient B) Average value of torque coefficient

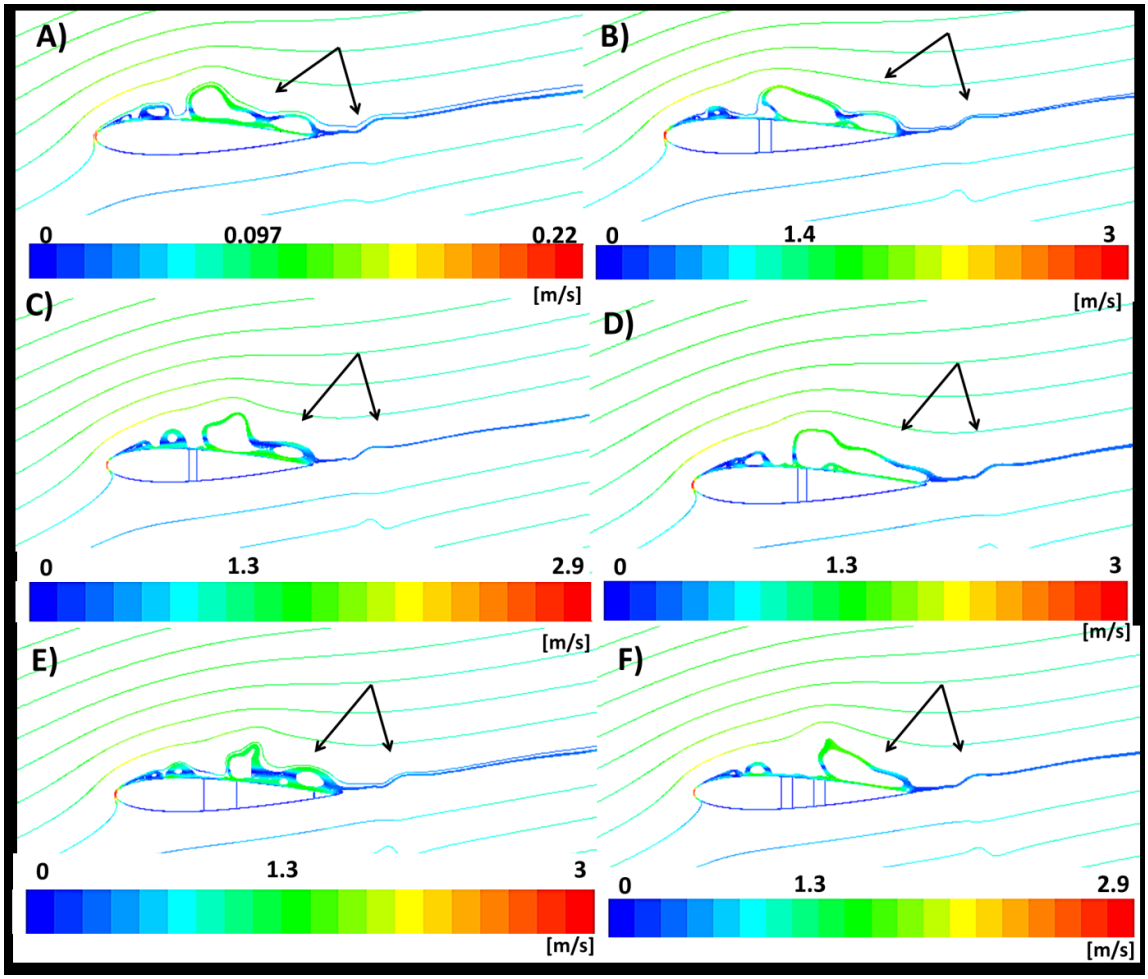

Figure 14 Path-line coloured by mean velocity magnitude at velocity equal to 1.8 m/s (acceleration flow) A) NACA0015 without slots B) L_{ss}40% and 45% C) L_{ss}40% and 44% D) L_{ss}45% and 49% E) L_{ss}40%, 55% and 90% F) L_{ss}40%,45%, 55%, and 60%

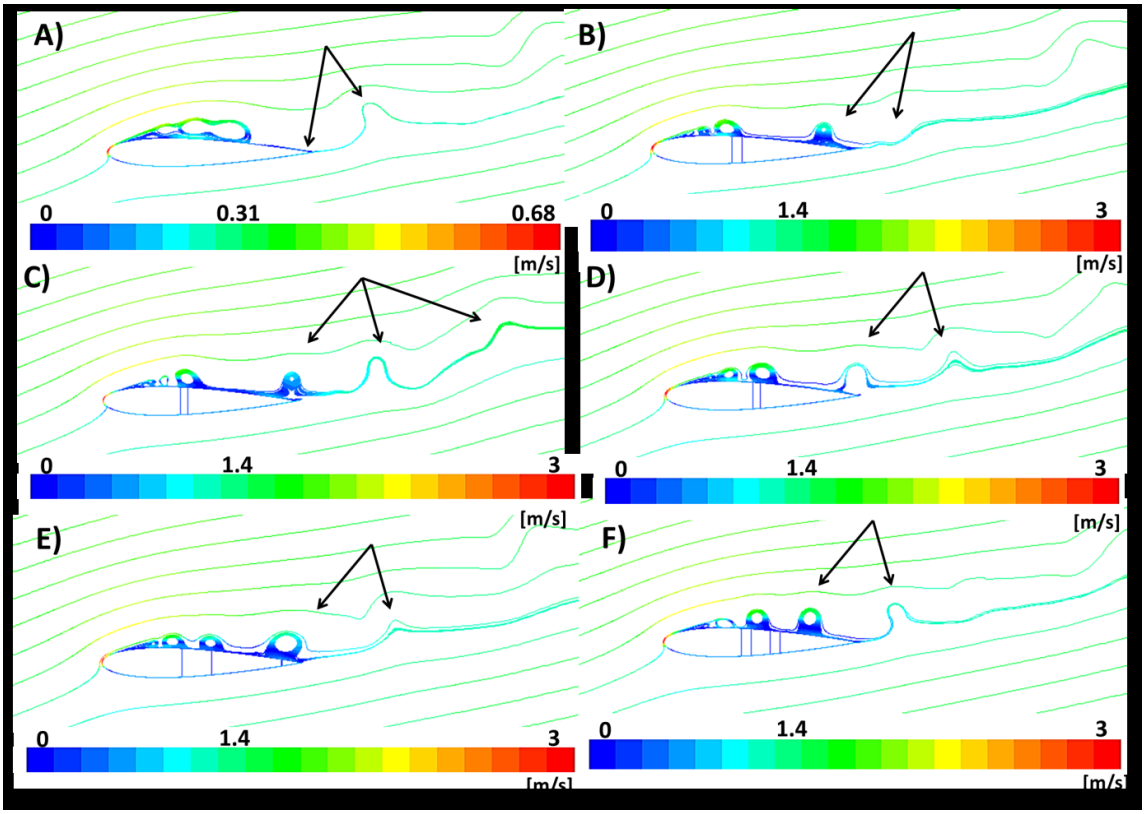

Figure 15 Path-line coloured by mean velocity magnitude at maximum velocity equal to 2.92 m/s A) NACA0015 without slots B) L_{ss}40% and 45% C) L_{ss}40% and 44% D) L_{ss}45% and 49% E) L_{ss}40%, 55% and 90% F) L_{ss}40%,45%, 55%, and 60%

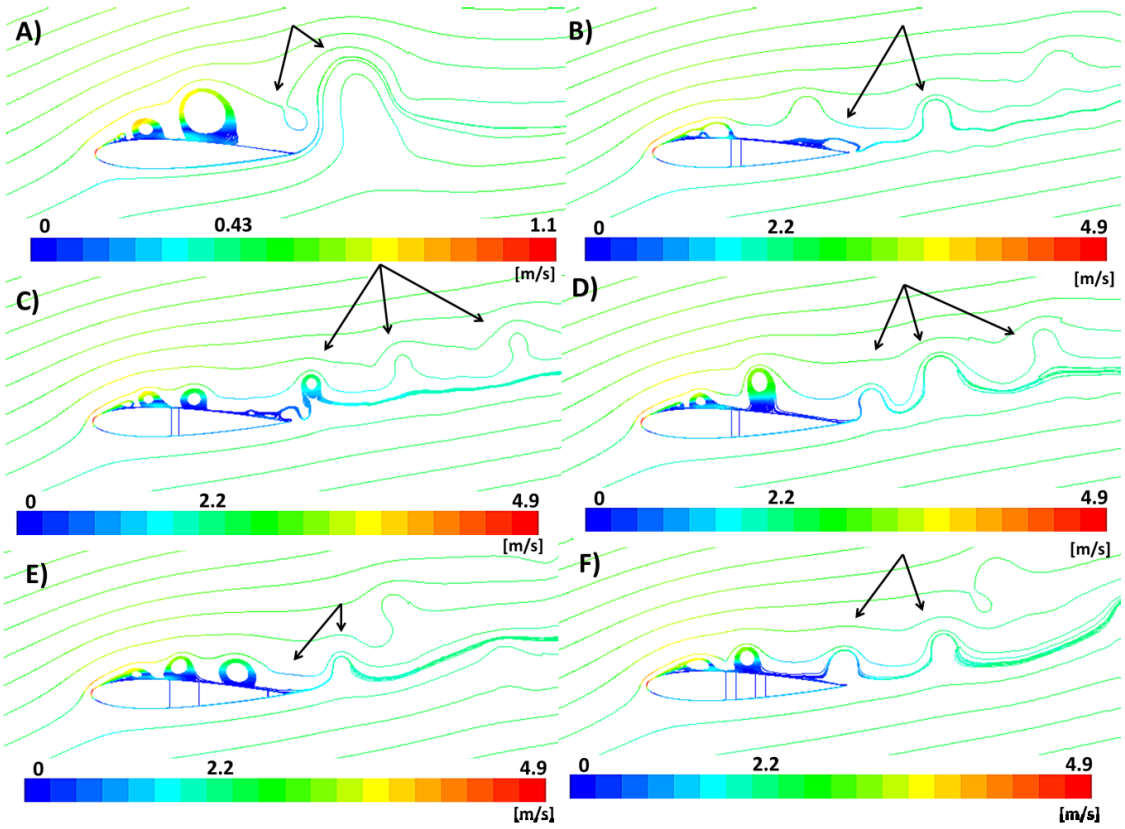

Figure 16 Path-line coloured by mean velocity magnitude at velocity equal to 1.8 m/s (deceleration flow), A) NACA0015 without slots B) L_{ss}40% and 45% C) L_{ss}40% and 44% D) L_{ss}45% and 49% E) L_{ss}40%, 55% and 90% F) L_{ss}40%,45%, 55%, and 60%

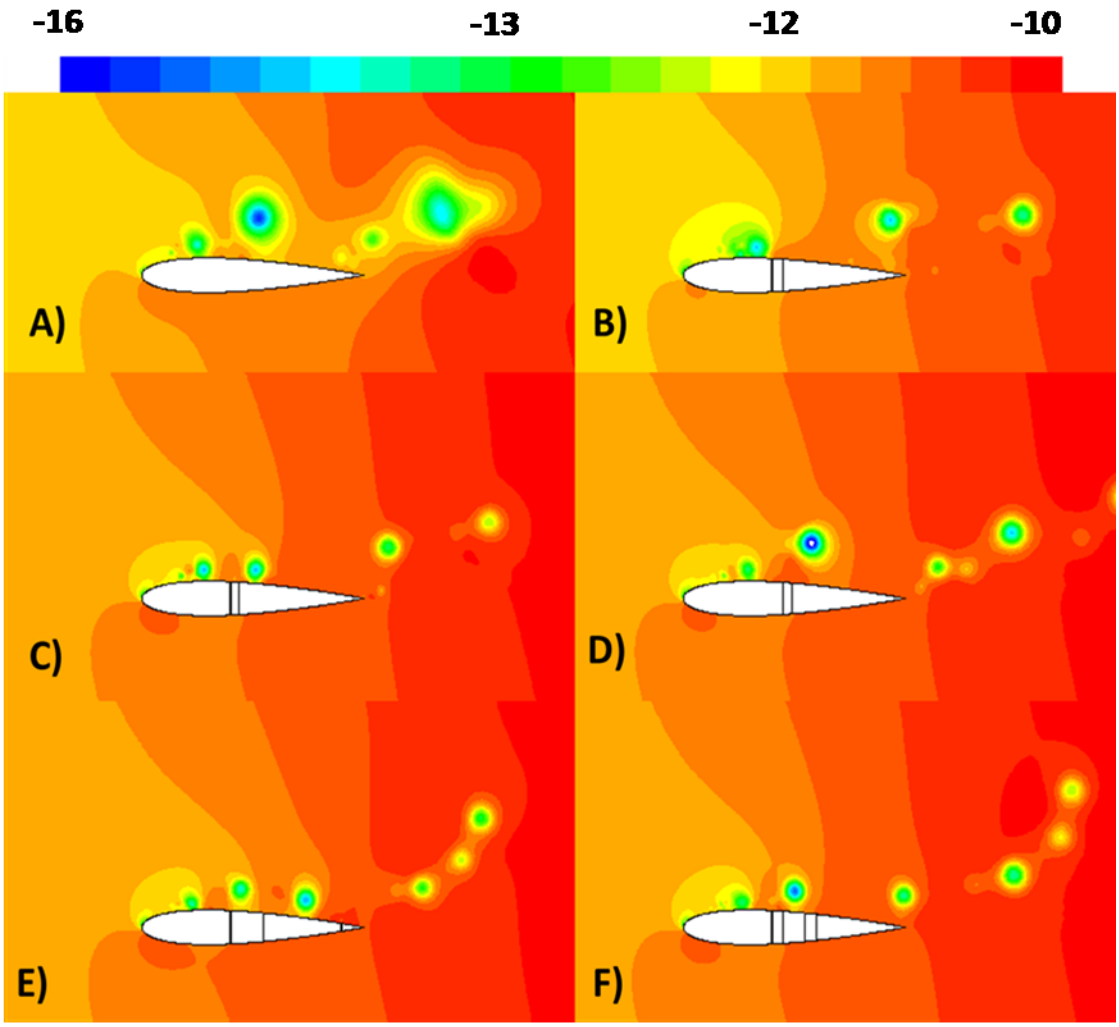

Figure 17 Contours coloured by pressure coefficient at velocity equal to 1.8 m/s (deceleration flow), A) NACA0015 without slots B) L_{ss}40% and 45% C) L_{ss}40% and 44% D) L_{ss}45% and 49% E) L_{ss}40%, 55% and 90% F) L_{ss}40%,45%, 55%, and 60%

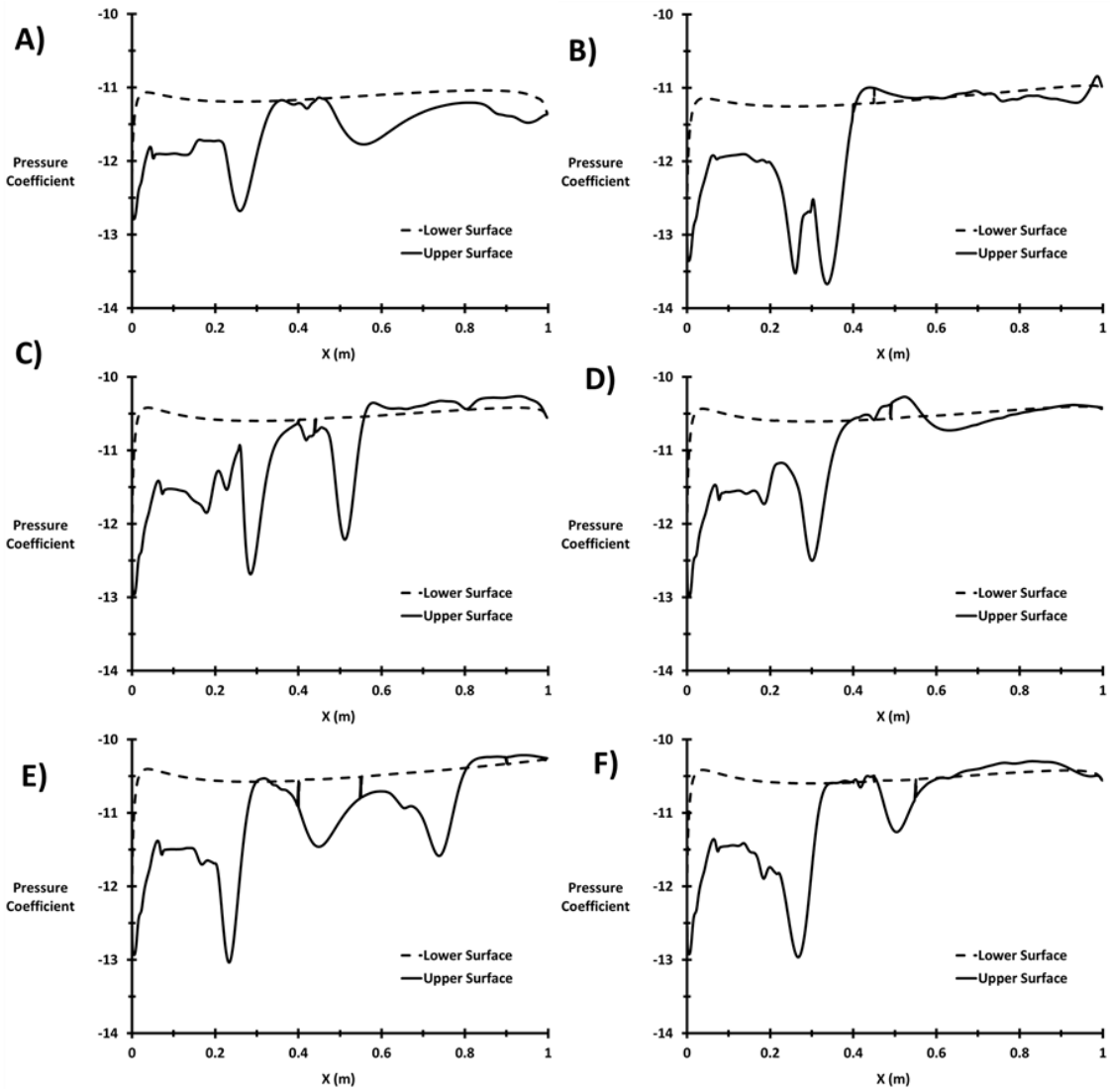

Figure 18 Pressure coefficient at upper and lower surface with velocity equal to 1.8 m/s (deceleration flow), A) NACA0015 without slots B) L_{ss}40% and 45% C) L_{ss}40% and 44% D) L_{ss}45% and 49% E) L_{ss}40%, 55% and 90% F) L_{ss}40%,45%, 55%, and 60%

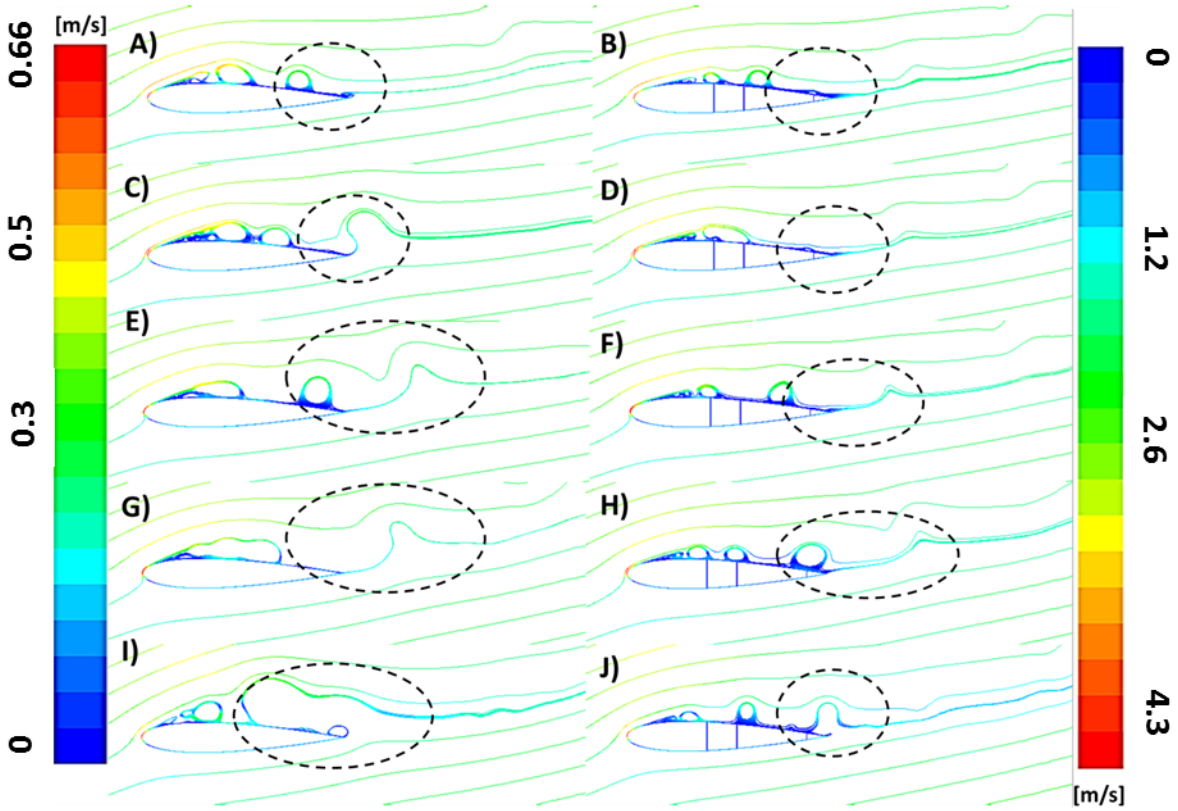

Figure 19 Path-line coloured by mean velocity magnitude around NACA0015 without and with slots at $\boldsymbol{L_{ss}}$40%, 55% and 90% at maximum velocity equal to 2.92 (m/s) A) and B) 11.3, C) and D) 11.7, E) and F) 12.3, G) and H) 13.6, I) and J) 14.4

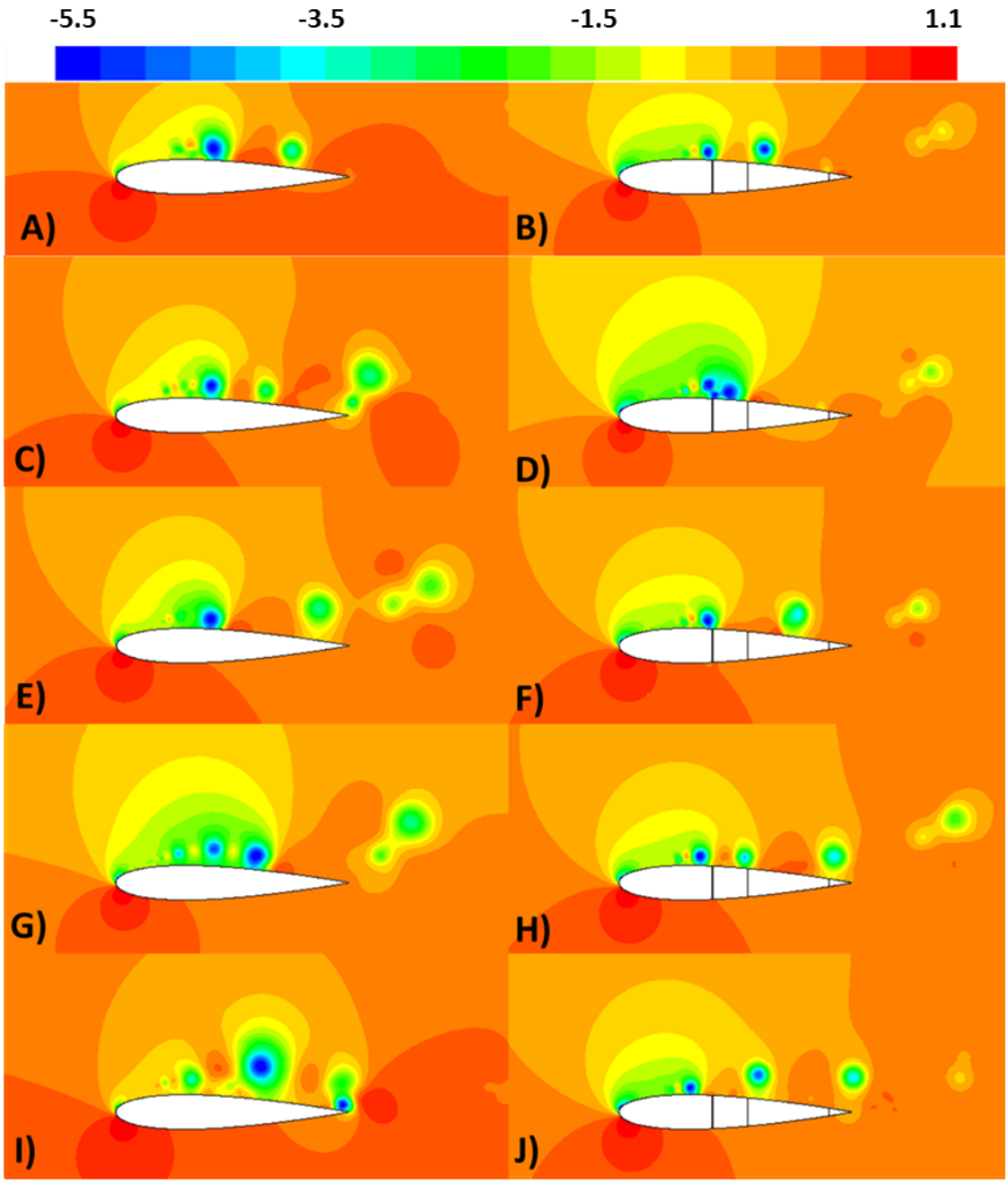

Figure 20 Contours of the pressure coefficient around NACA0015 A) and B) 11.3, C) and D) 11.7, E) and F) 12.3, G) and H) 13.6, I) and J) 14.4

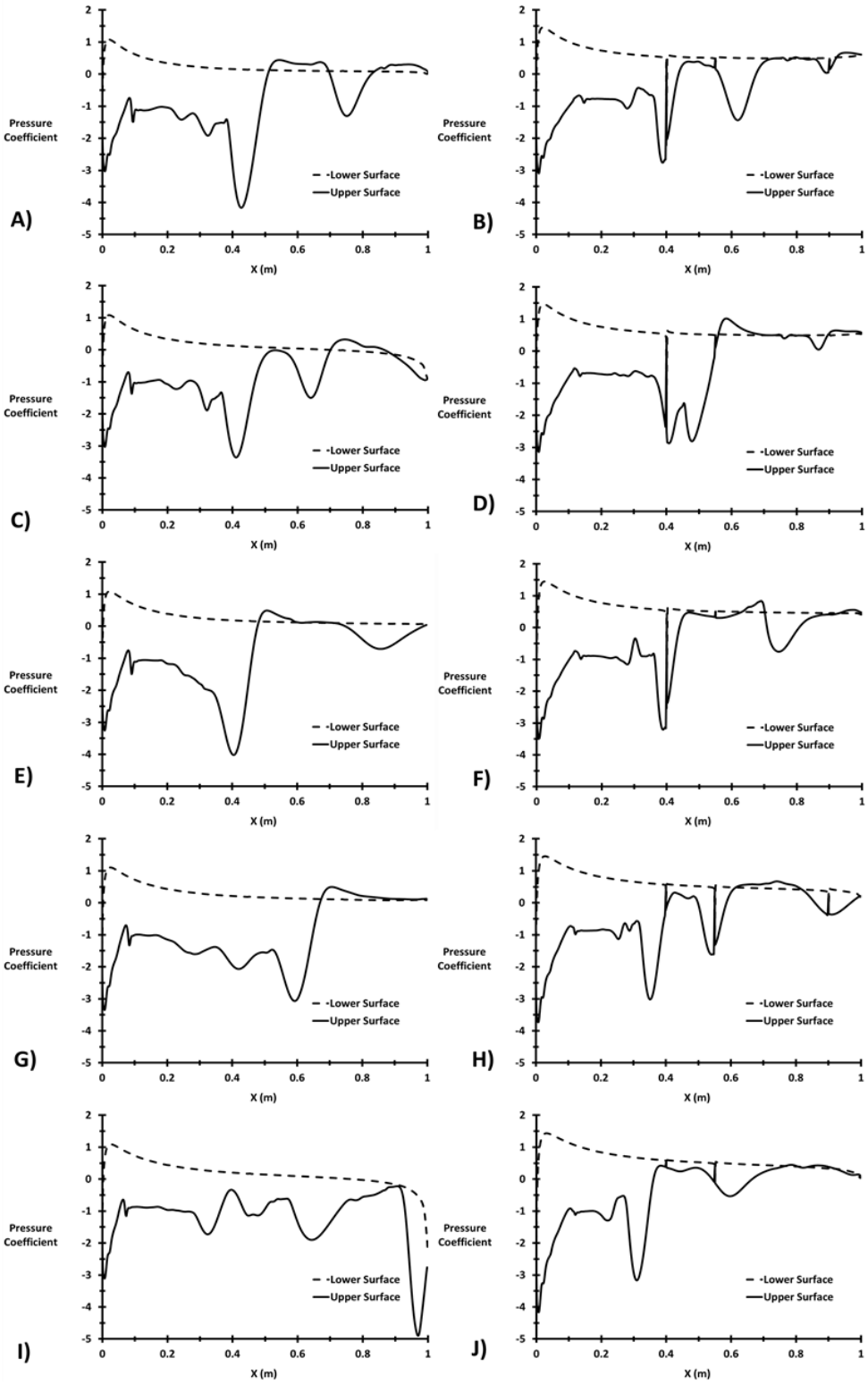

Figure 21 Pressure coefficient at upper and lower surface of NACA0015 A) and B) 11.3, C) and D) 11.7, E) and F) 12.3, G) and H) 13.6, I) and J) 14.4

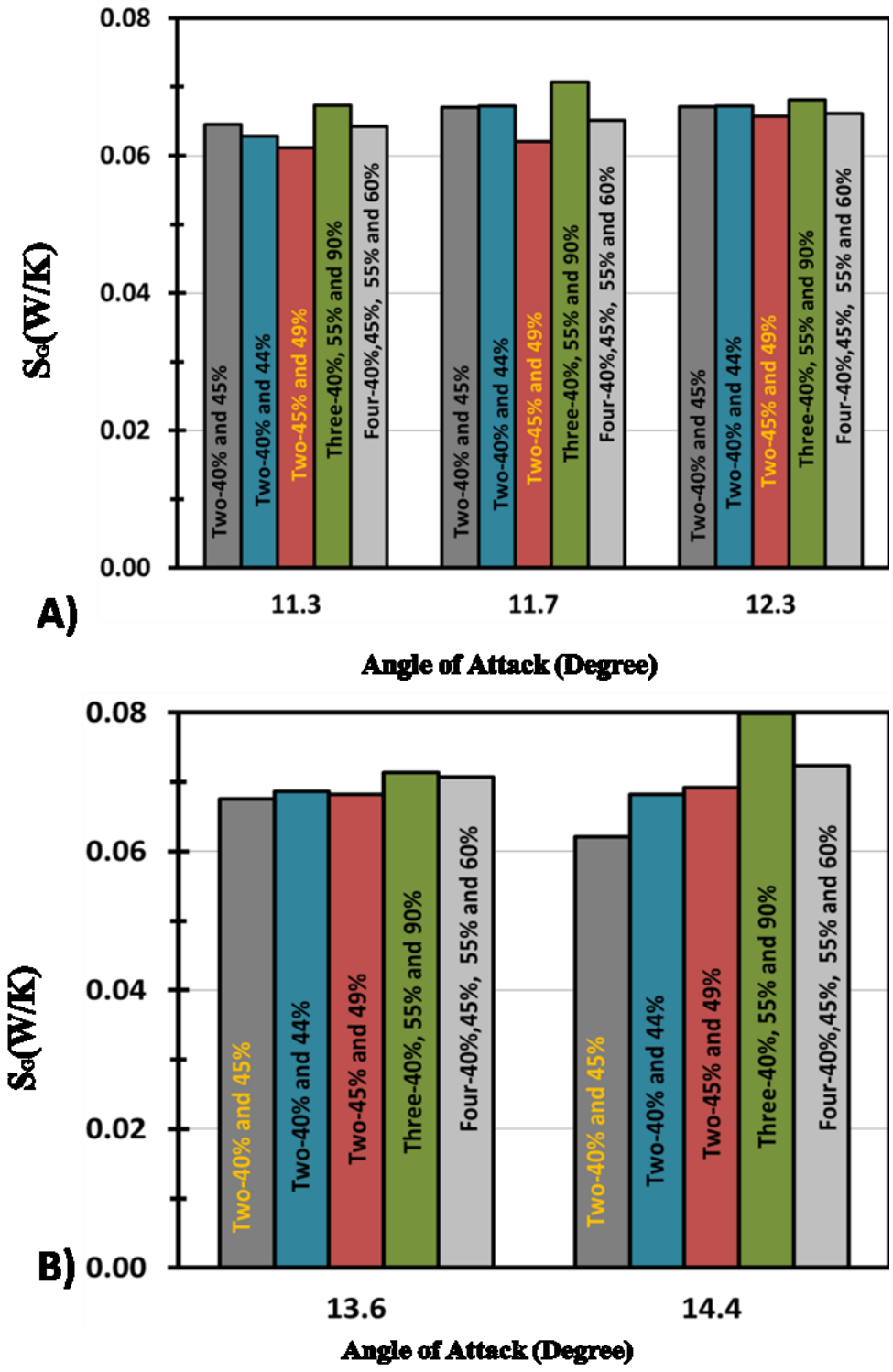

Figure 22 Comparison between the average value of the S_G for the compression cycle for NACA0015 with two, three and four suction slots, A) Before the stall B) After the stall

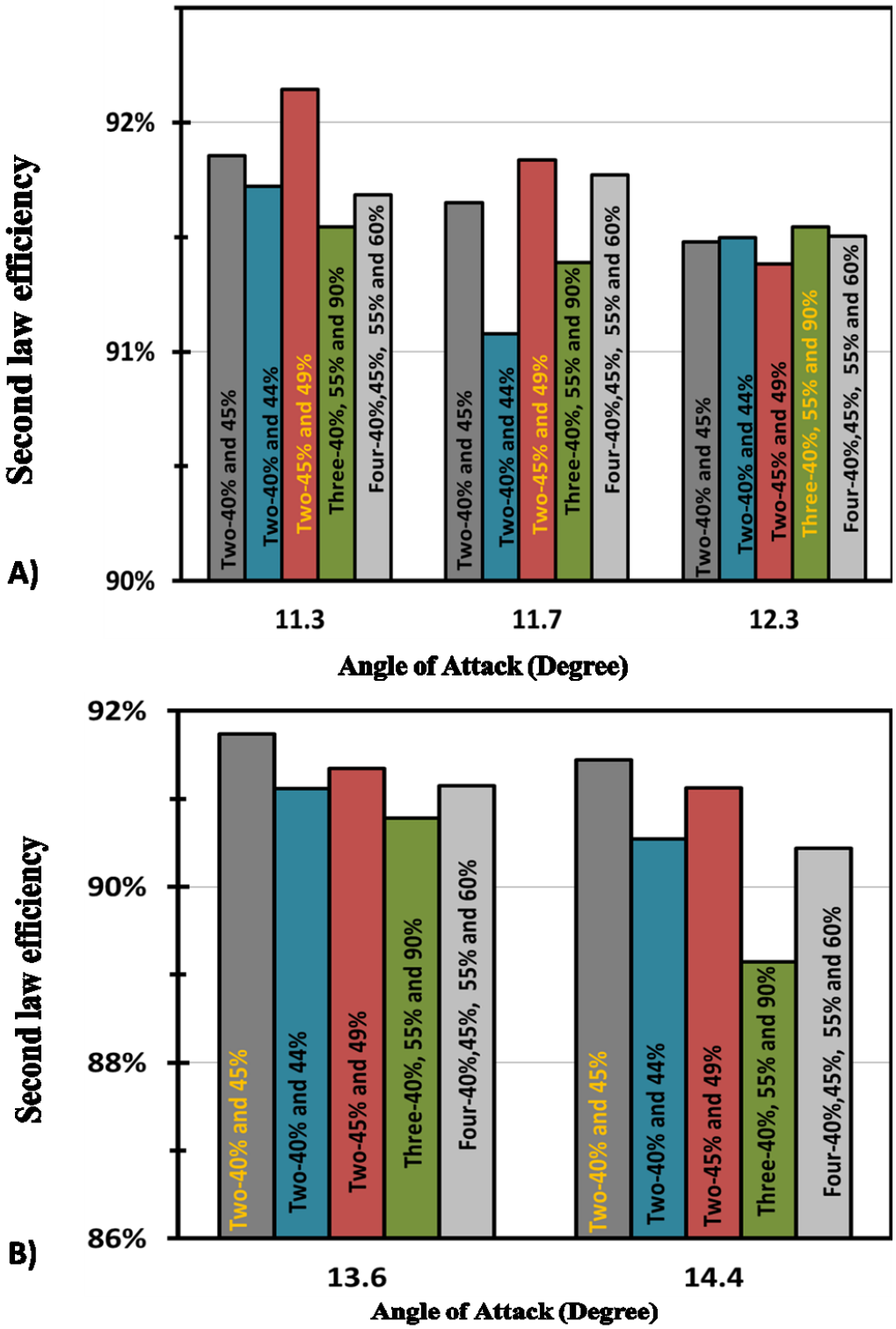

Figure 23 Comparison between the second law efficiency for the compression cycle for NACA0015 with two, three and four suction slots A) Before the stall B) After the stall

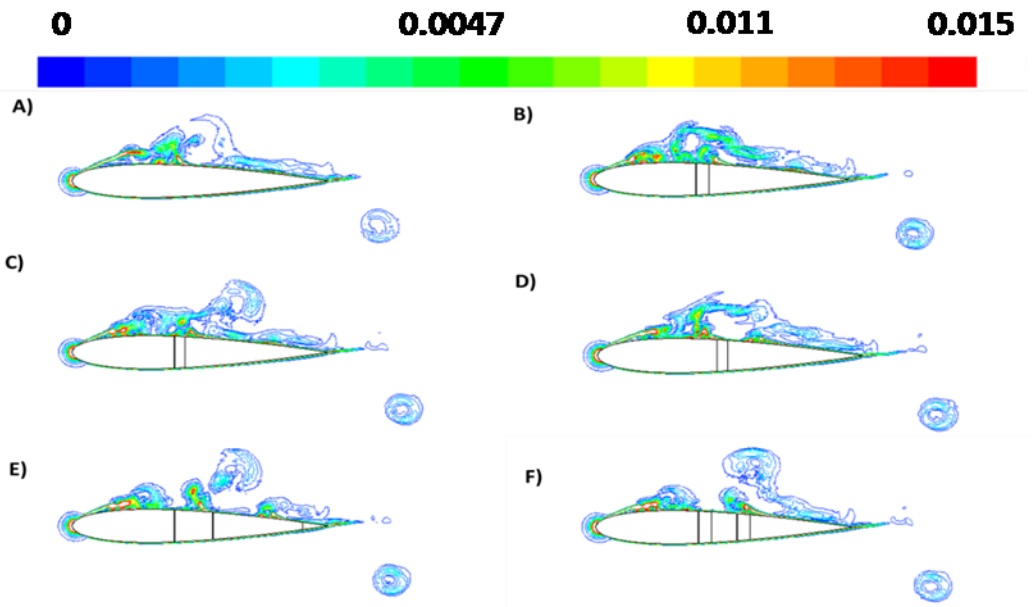

Figure 24 Contour of S_G at 1.8 m/s (accelerating) A) NACA0015 without slots B) L_{ss}40% and 45% C) L_{ss}40% and44% D) L_{ss}45% and 49% E) L_{ss}40%, 55% and 90% F) L_{ss}40%,45%, 55%, and 60%

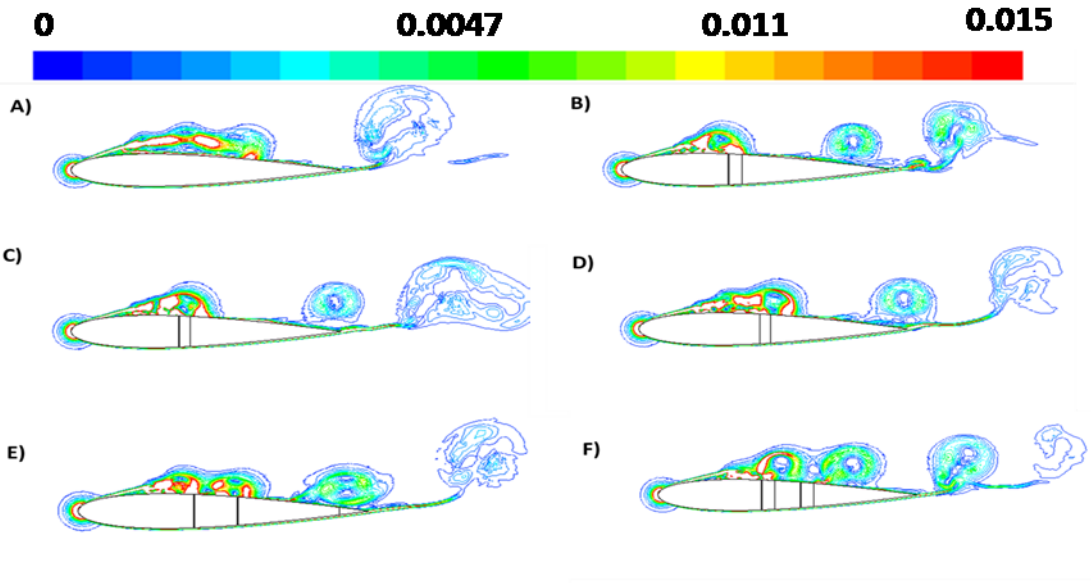

Figure 25 Contour of S_G at 2.92 m/s (maximum velocity) A) NACA0015 without suction slots B) L_{ss}40% and 45% C) L_{ss}40% and 44% D) L_{ss}45% and 49% E) L_{ss}40%, 55% and 90% F) L_{ss}40%,45%, 55%, and 60%

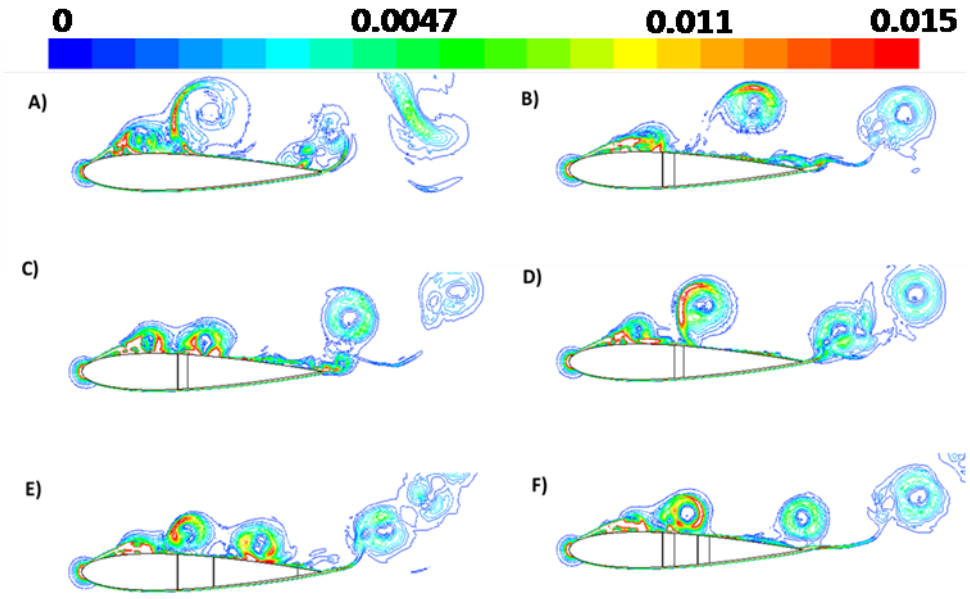

Figure 26 Contour of S_G at 1.8 m/s (decelerating) A) NACA0015 without slots B) L_{ss}40% and 45% C) L_{ss}40% and 44% D) L_{ss}45% and 49% E) L_{ss}40%, 55% and 90% F) L_{ss}40%, 45%, 55%, and 60%

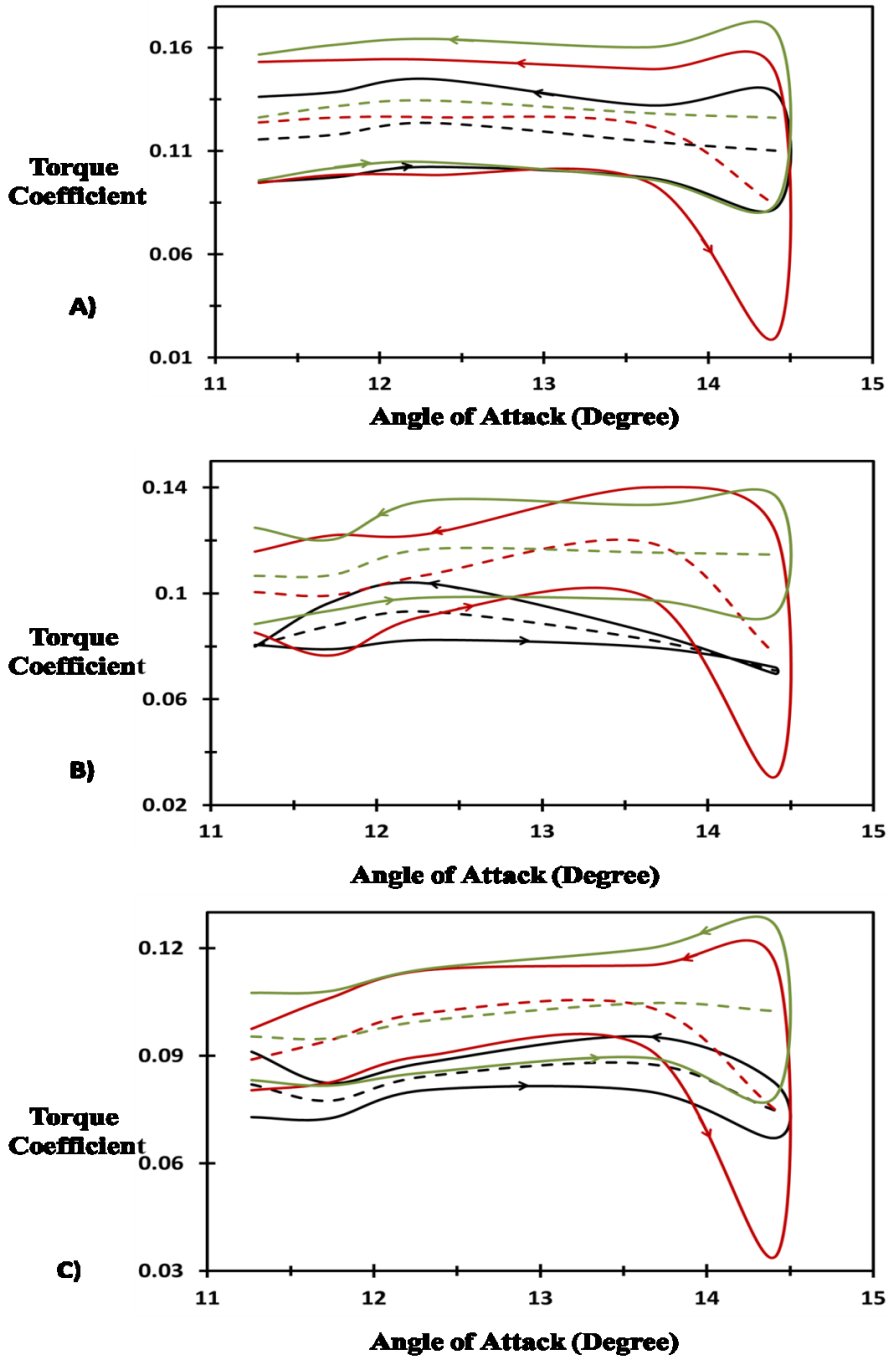

Figure 27 The hysteretic behaviour and the average torque coefficient "—— without slots ---average value", "—— (L_{ss}40% and 45%) ---average value", "—— (L_{ss}40%, 55% and 90%) ---average value", A) t_{sin} = 4 sec B) t_{sin} = 6 sec C) t_{sin} = 8 sec

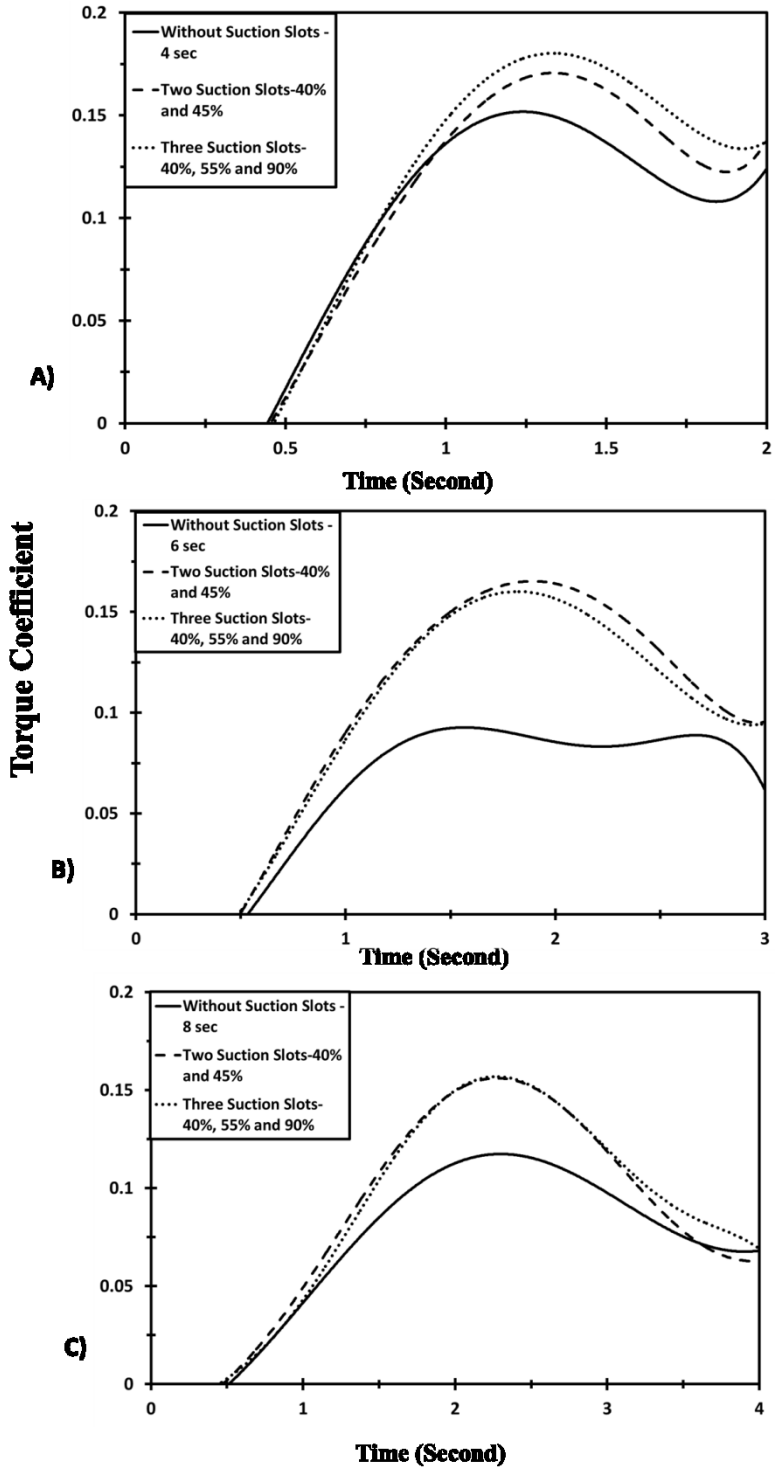

Figure 28 The instantaneous torque coefficient for the NACA0015 without and with suction slots at optimum locations in 13.6 º A) t_{sin} = 4 sec B) t_{sin} = 6 sec C) t_{sin} = 8 sec

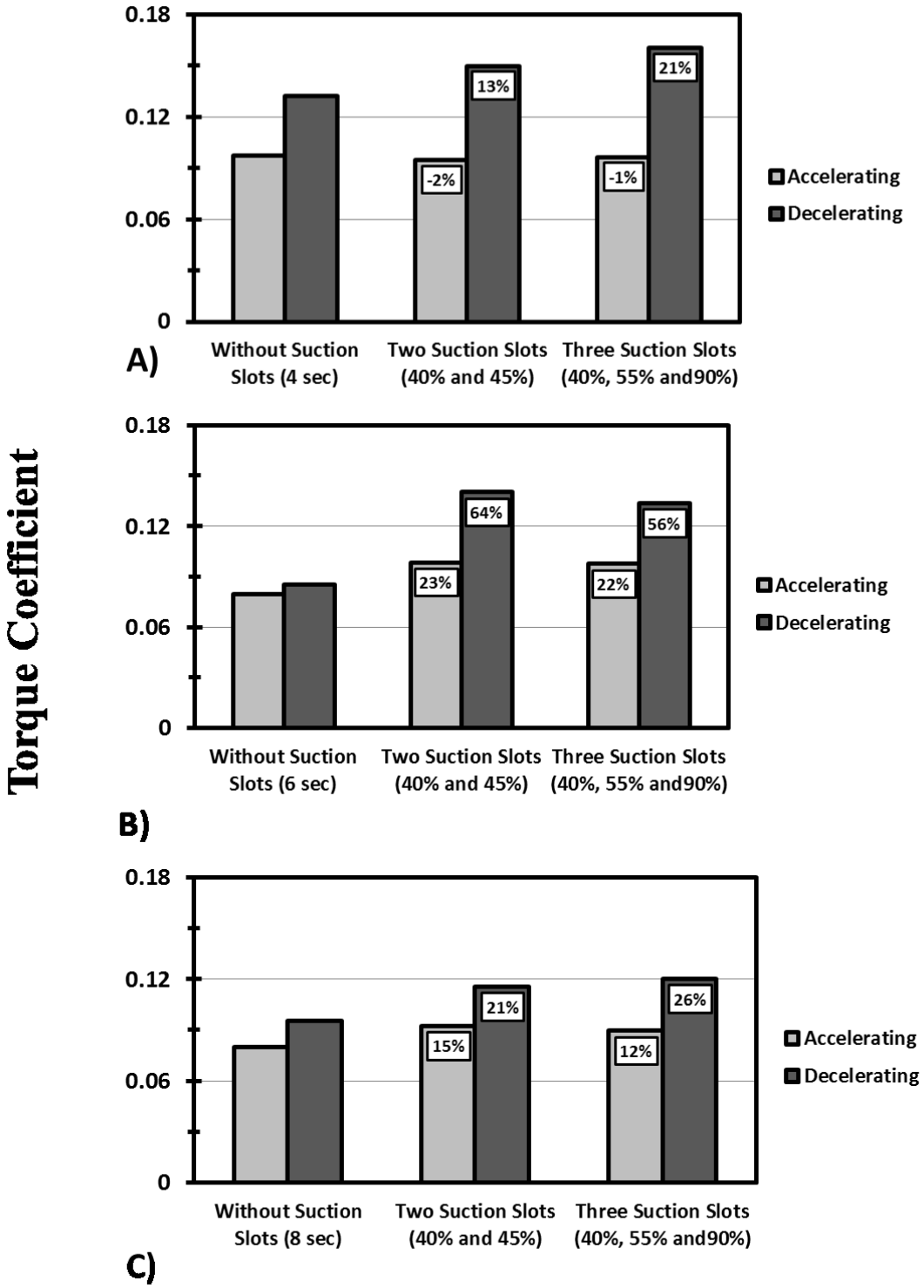

Figure 29 The average torque coefficient at the accelerating and decelerating flow for the NACA0015 without and with suction slots at optimum locations A) t_{sin} = 4 sec B) t_{sin} = 6 sec C) t_{sin} = 8 sec

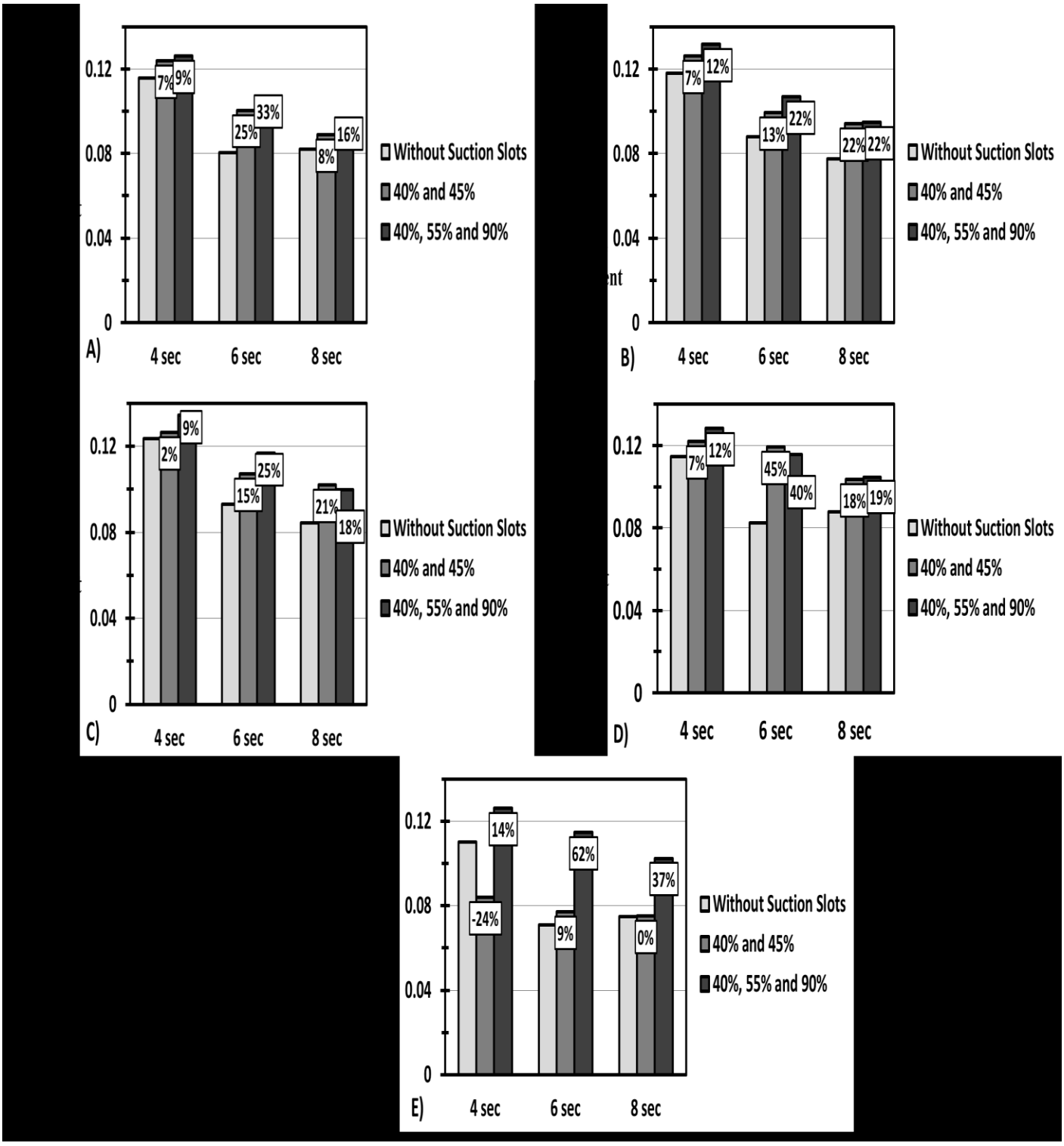

Figure 30 The average torque coefficient at the compression cycle for the NACA0015 without and with suction slots at optimum locations with sinusoidal velocity A) 11.3 B) 11.7 C) 12.3 D) 13.6 E) 14.4

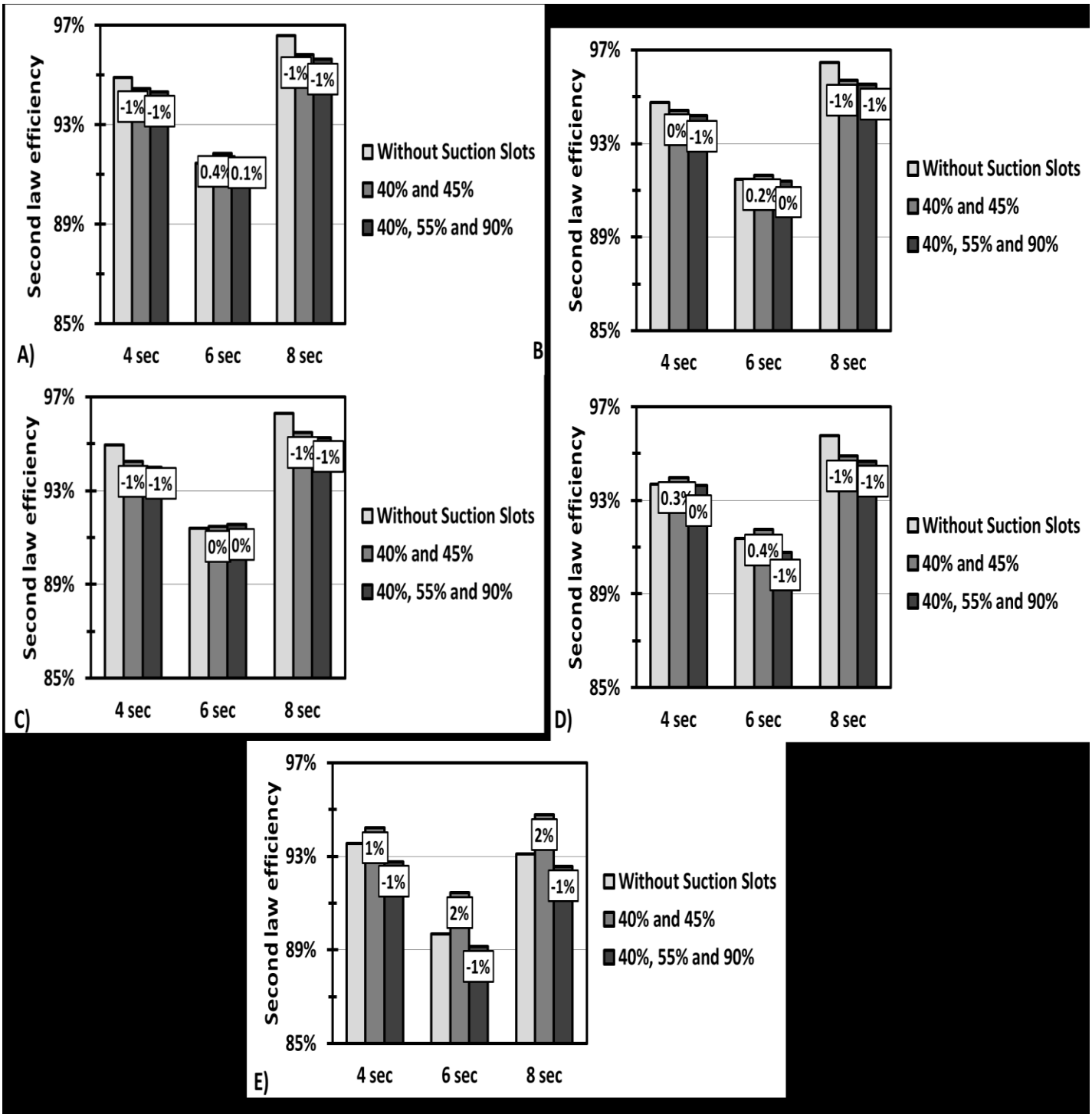

Figure 31 The second law efficiency at the compression cycle for the NACA0015 without and with suction slots at optimum locations with sinusoidal velocity A) 11.3 B) 11.7 C) 12.3 D) 13.6 E) 14.4

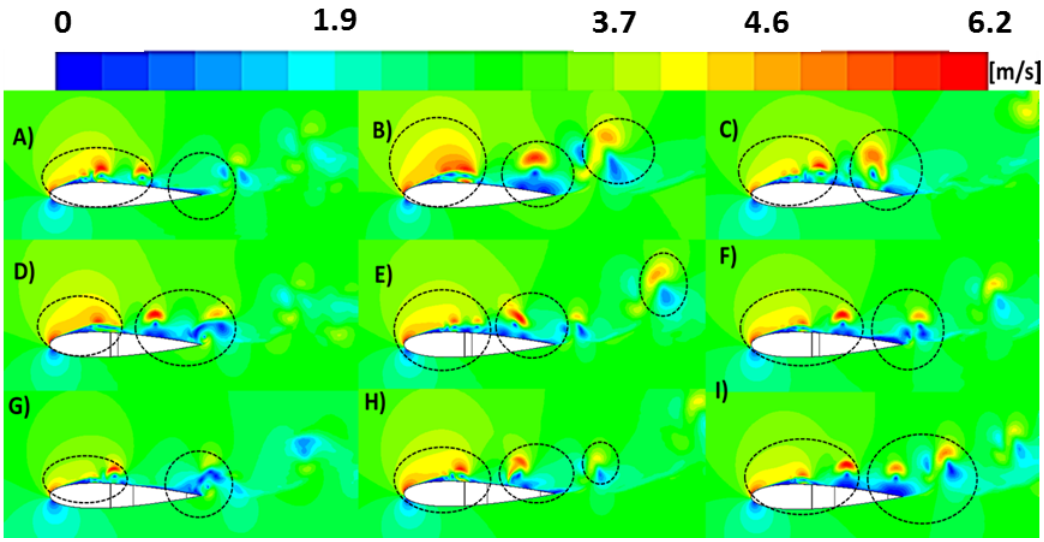

Figure 32 Contour of velocity magnitude at 12.3 ° A), B) and C) NACA0015 without slots with t_{sin} = 4, 6 and 8 sec respectively D), E) and F) two slots with t_{sin} = 4, 6 and 8 sec respectively G), H) and I) three slots with t_{sin} = 4, 6 and 8 sec respectively

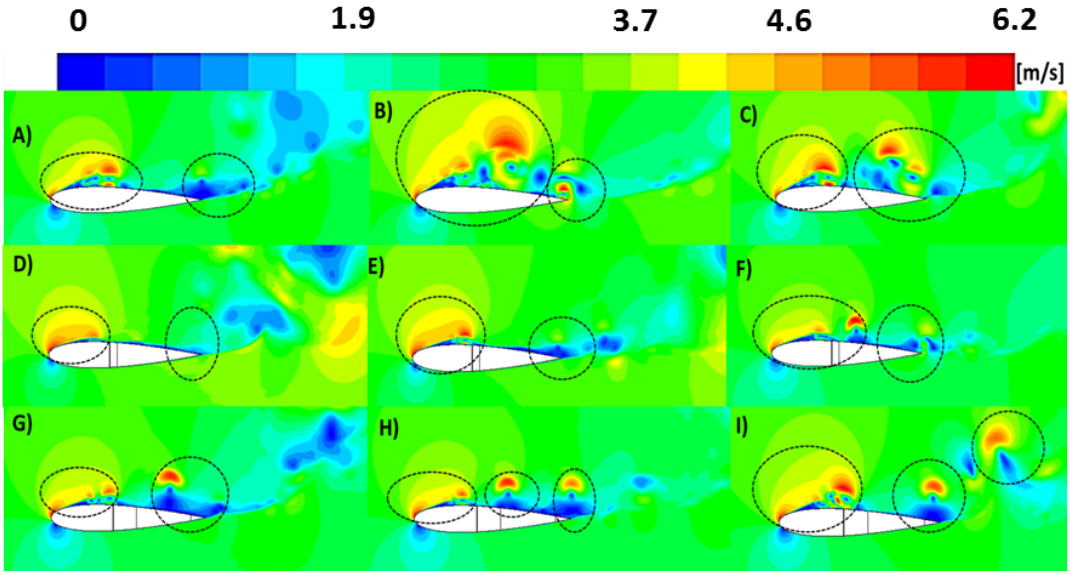

Figure 33 Contour of velocity magnitude at 14.4 ° A), B) and C) for NACA0015 without slots with t_{sin} = 4, 6 and 8 sec respectively D), E) and F) two slots with t_{sin} = 4, 6 and 8 sec respectively G), H) and I) three slots with t_{sin} = 4, 6 and 8 sec respectively